














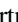















# Transmission Spectroscopy for the Warm Sub-Neptune HD 3167c: Evidence for Molecular Absorption and a Possible High-metallicity Atmosphere

Thomas Mikal-Evans<sup>1</sup> , Ian J. M. Crossfield<sup>2</sup>, Björn Benneke<sup>3</sup> , Laura Kreidberg<sup>4,5</sup> , Julie Moses<sup>6</sup> , Caroline V. Morley<sup>7</sup> , Daniel Thorngren<sup>8</sup> , Paul Mollière<sup>9</sup> , Kevin K. Hardegree-Ullman<sup>10</sup> , John Brewer<sup>11</sup> , Jessie L. Christiansen<sup>10</sup> , David R. Ciardi<sup>10</sup> , Diana Dragomir<sup>12</sup> , Courtney Dressing<sup>13</sup> , Jonathan J. Fortney<sup>14</sup> , Varoujan Gorjian<sup>15</sup> , Thomas P. Greene<sup>16</sup> , Lea A. Hirsch<sup>17</sup> , Andrew W. Howard<sup>18</sup> , Steve B. Howell<sup>19</sup> , Howard Isaacson<sup>20,21</sup> , Molly R. Kosiarek<sup>14,26</sup> , Jessica Krick<sup>10</sup> , John H. Livingston<sup>22</sup> , Joshua D. Lothringer<sup>23</sup> , Farisa Y. Morales<sup>15</sup> , Erik A. Petigura<sup>24</sup> , Joshua E. Schlieder<sup>25</sup> , and Michael Werner<sup>15</sup>

<sup>1</sup> Kavli Institute for Astrophysics and Space Research, Massachusetts Institute of Technology, Cambridge, MA, USA; [tmevans@mit.edu](mailto:tmevans@mit.edu)

<sup>2</sup> Department of Physics and Astronomy, University of Kansas, Lawrence, KS, USA

<sup>3</sup> Département de Physique, and Institute for Research on Exoplanets, Université de Montréal, Montréal, QC, Canada

<sup>4</sup> Max Planck Institute for Astronomy, Königstuhl 17, D-69117 Heidelberg, Germany

<sup>5</sup> Center for Astrophysics, Harvard & Smithsonian, 60 Garden Street, Cambridge, MA, 02138, USA

<sup>6</sup> Space Science Institute, 4765 Walnut St. Suite B, Boulder, CO 80301, USA

<sup>7</sup> Department of Astronomy, University of Texas at Austin, Austin, TX 78712, USA

<sup>8</sup> Institute for Research on Exoplanets (iREx), Université de Montréal, Montréal, QC, Canada

<sup>9</sup> Max-Planck-Institut für Astronomie, Königstuhl 17, D-69117 Heidelberg, Germany

<sup>10</sup> Caltech/IPAC, M/S 100-22, 1200 E. California Blvd., Pasadena, CA 91125, USA

<sup>11</sup> Department of Physics and Astronomy, San Francisco State University, 1600 Holloway Ave., San Francisco, CA 94132, USA

<sup>12</sup> Department of Physics and Astronomy, University of New Mexico, 1919 Lomas Blvd. NE, Albuquerque, NM 87131, USA

<sup>13</sup> Department of Astronomy, University of California Berkeley, Berkeley, CA 94720, USA

<sup>14</sup> Department of Astronomy & Astrophysics, University of California, Santa Cruz, CA 95064, USA

<sup>15</sup> Jet Propulsion Laboratory, California Institute of Technology, Pasadena, CA, USA

<sup>16</sup> Space Science and Astrobiology Division, NASA Ames Research Center, MS 245-6, Moffett Field, CA 94035, USA

<sup>17</sup> Kavli Institute for Particle Astrophysics and Cosmology, Stanford University, Stanford, CA 94305, USA

<sup>18</sup> Department of Astronomy, California Institute of Technology, Pasadena, CA 91125, USA

<sup>19</sup> NASA Ames Research Center, Moffett Field, CA 94035, USA

<sup>20</sup> Astronomy Department, University of California, Berkeley, CA, USA

<sup>21</sup> University of Southern Queensland, Toowoomba, QLD 4350, Australia

<sup>22</sup> Department of Astronomy, University of Tokyo, 7-3-1 Hongo, Bunkyo-ku, Tokyo 113-0033, Japan

<sup>23</sup> Department of Physics and Astronomy, Johns Hopkins University, Baltimore, MD 21210, USA

<sup>24</sup> Department of Physics & Astronomy, University of California Los Angeles, Los Angeles, CA 90095, USA

<sup>25</sup> Exoplanets and Stellar Astrophysics Laboratory, Code 667, NASA Goddard Space Flight Center, Greenbelt, MD 20771, USA

Received 2020 July 31; revised 2020 October 19; accepted 2020 November 5; published 2020 December 7

## Abstract

We present a transmission spectrum for the warm (500–600 K) sub-Neptune HD 3167c obtained using the Hubble Space Telescope Wide Field Camera 3 infrared spectrograph. We combine these data, which span the 1.125–1.643  $\mu\text{m}$  wavelength range, with broadband transit measurements made using Kepler/K2 (0.6–0.9  $\mu\text{m}$ ) and Spitzer/IRAC (4–5  $\mu\text{m}$ ). We find evidence for absorption by at least one of H<sub>2</sub>O, HCN, CO<sub>2</sub>, and CH<sub>4</sub> (Bayes factor 7.4; 2.5 $\sigma$  significance), although the data precision does not allow us to unambiguously discriminate between these molecules. The transmission spectrum rules out cloud-free hydrogen-dominated atmospheres with metallicities  $\leq 100\times$  solar at  $>5.8\sigma$  confidence. In contrast, good agreement with the data is obtained for cloud-free models assuming metallicities  $>700\times$  solar. However, for retrieval analyses that include the effect of clouds, a much broader range of metallicities (including subsolar) is consistent with the data, due to the degeneracy with cloud-top pressure. Self-consistent chemistry models that account for photochemistry and vertical mixing are presented for the atmosphere of HD 3167c. The predictions of these models are broadly consistent with our abundance constraints, although this is primarily due to the large uncertainties on the latter. Interior structure models suggest that the core mass fraction is  $>40\%$ , independent of a rock or water core composition, and independent of atmospheric envelope metallicity up to  $1000\times$  solar. We also report abundance measurements for 15 elements in the host star, showing that it has a very nearly solar composition.

*Unified Astronomy Thesaurus concepts:* [Exoplanet astronomy \(486\)](#); [Exoplanets \(498\)](#); [Exoplanet atmospheres \(487\)](#)

## 1. Introduction

The Hubble Space Telescope (HST) has proven a productive facility for characterizing the atmospheres of transiting exoplanets. Observational studies released since 2019 alone include Arcangeli et al. (2019), Benneke et al. (2019a, 2019b),

Chachan et al. (2019), dos Santos et al. (2019), Mikal-Evans et al. (2019, 2020), Sing et al. (2019), Spake et al. (2019), Guo et al. (2020), Wong et al. (2020), Alam et al. (2020), Fu et al. (2020), Wakeford et al. (2020), Carter et al. (2020), Bruno et al. (2020), Sotzen et al. (2020), Carone et al. (2020), Kreidberg et al. (2020), and Colón et al. (2020). Transmission spectroscopy measurements, made during primary transit, allow the

<sup>26</sup> NSF Graduate Student Research Fellowship.

composition of the day–night terminator atmosphere to be probed, while at other phases in the orbit when the irradiated dayside hemisphere is visible, the planetary emission can be constrained (for overviews, see Deming & Seager 2017; Deming et al. 2019). Most HST transmission and emission spectroscopy observations have been performed using either the Space Telescope Imaging Spectrograph (STIS) at near-UV/optical wavelengths (e.g., Sing et al. 2019; Alam et al. 2020; Fu et al. 2020) or Wide Field Camera 3 (WFC3) at near-infrared wavelengths (e.g., Arcangeli et al. 2019; Benneke et al. 2019a, 2019b; Mikal-Evans et al. 2019, 2020; Carter et al. 2020). To date, published observations have mainly focused on hot Jupiters, which are especially favorable targets owing to their large radii and high temperatures (e.g., Sing et al. 2016). However, the NASA Kepler survey revealed that planets Neptune sized and smaller ( $\lesssim 4 R_{\oplus}$ ) are far more common than the hot Jupiters, with an abundance distribution that rises with increasing semimajor axis out to orbital periods of at least 100 days (Howard et al. 2010; Dressing & Charbonneau 2013; Fressin et al. 2013; Petigura et al. 2013; Foreman-Mackey et al. 2014). Characterizing the atmospheres of these smaller and cooler planets, although relatively challenging, is therefore key to our overall understanding of the planetary population.

The observed size distribution of planets smaller than Neptune exhibits a distinct minimum, or “radius valley,” centered around  $\sim 1.8 R_{\oplus}$  for orbital periods shorter than 100 days (Rogers 2015; Fulton et al. 2017; van Eylen et al. 2018; Cloutier & Menou 2020). The super-Earths fall below this valley, with bulk density measurements indicating predominantly rocky compositions (Weiss & Marcy 2014). Any H/He atmospheres these close-in super-Earths may have accreted from the protoplanetary nebula during formation must have been lost, likely by thermal escape (e.g., Lopez & Fortney 2013, 2014; Zahnle & Catling 2017). For sub-Neptunes with radii above the valley, there is more ambiguity, as their masses and radii can be explained by various proportions of iron, rock, water, and H/He (e.g., Valencia et al. 2007, 2013; Adams et al. 2008; Rogers & Seager 2010a, 2010b; Howe et al. 2014; Dorn et al. 2017; Baumeister et al. 2020). One possibility is that most of these sub-Neptunes possess rock/iron cores and are surrounded by thick H/He envelopes contributing  $\sim 1\%$ – $10\%$  of the total planet mass (Lopez & Fortney 2013, 2014; Jin & Mordasini 2018). A number of popular theories posit that many of the rocky planets below the radius valley are in fact the exposed cores of such “gas dwarfs,” with primordial H/He atmospheres stripped by processes that may include photoevaporation and core-powered mass loss (Owen & Wu 2013, 2017; Gupta & Schlichting 2019). Under this scenario, the sub-Neptunes are planets drawn from the same initial population, only they managed to retain their H/He envelopes. An alternative suggestion is that many of the sub-Neptunes could instead be composed of rock and water in comparable proportions, with little or no H/He (Zeng et al. 2019; Mousis et al. 2020). Such worlds would need to form beyond the snow line, where water ice is abundant, and subsequently migrate to their present close-in orbits. Adding further intrigue to the sub-Neptunes, population synthesis simulations are now capable of reproducing many of the properties of the observed exoplanet sample but continue to significantly underpredict the frequency of sub-Neptunes (Mulders et al. 2019). Clearly, there is much remaining to be learned about how the sub-Neptunes form and what they are

composed of, which is all the more significant given the prominent place they occupy in the planetary population.

Transmission spectroscopy observations performed with HST provide a means of directly probing the atmospheric compositions for the most favorable sub-Neptunes. To date, there have been HST transmission spectra published for only four such targets with radii  $\sim 1.8$ – $4 R_{\oplus}$ : GJ 1214b (Berta et al. 2012; Kreidberg et al. 2014), HD 97658b (Knutson et al. 2014b; Guo et al. 2020), 55 Cnc e (Tsiaras et al. 2016), and K2-18b (Benneke et al. 2019b). There have also been four HST transmission spectra published for planets with radii somewhat larger than Neptune ( $\sim 4$ – $5 R_{\oplus}$ ): GJ 436b (Knutson et al. 2014a; Lothringer et al. 2018), HAT-P-11b (Fraigne et al. 2014; Chachan et al. 2019), GJ 3470b (Ehrenreich et al. 2014; Benneke et al. 2019a), and HD 106315c (Kreidberg et al. 2020). Of this combined sample, most have produced detections of spectral features at varying levels of confidence (Crossfield & Kreidberg 2017a). In particular, statistically strong H<sub>2</sub>O detections have been made for HAT-P-11b (Fraigne et al. 2014), GJ 3470b (Benneke et al. 2019a), and K2-18b (Benneke et al. 2019b). A more tentative H<sub>2</sub>O detection has recently been reported for HD 106315c (Kreidberg et al. 2020), while HD 97658b shows indications of spectral features, although the interpretation remains uncertain (Guo et al. 2020). For 55 Cnc e—which, with a radius of  $1.897^{+0.044}_{-0.046} R_{\oplus}$  (Dai et al. 2019), falls at the borderline of the super-Earth and sub-Neptune regimes—Tsiaras et al. (2016) claimed the detection of a thick atmosphere containing HCN. Only GJ 1214b and GJ 436b have failed to produce spectral feature detections. A deck of obscuring cloud or photochemical haze is required to explain the GJ 1214b spectrum (Kreidberg et al. 2014), while for GJ 436b the available data favor high-metallicity scenarios ( $>600\times$  solar; Morley et al. 2017) but are not precise enough to resolve small-amplitude spectral features and rule out a cloud deck.

In this paper, we present a transmission spectrum for the sub-Neptune HD 3167c measured with HST WFC3, combined with transit photometry obtained with Kepler K2 and the Spitzer Space Telescope Infrared Array Camera (IRAC). The HD 3167 system comprises a bright ( $J = 7.5$  mag,  $K = 7.1$  mag) early K-type dwarf located approximately 47 pc away (Gaia Collaboration et al. 2018), orbited by at least three planets. Two of the known planets transit the host star and were first discovered in K2 photometry by Vanderburg et al. (2016), while the third was detected by radial velocity follow-up measurements and does not transit (Christiansen et al. 2017; Gandolfi et al. 2017). Our target, HD 3167c, is the outermost of these planets, with a semimajor axis of  $\sim 0.18$  au and an equilibrium temperature of  $T_{\text{eq}} \sim 500$ – $600$  K. It falls squarely in the sub-Neptune regime, with measured mass  $9.80^{+1.30}_{-1.24} M_{\oplus}$  and radius  $3.01^{+0.42}_{-0.28} R_{\oplus}$  (Christiansen et al. 2017). The innermost planet (HD 3167b) is a super-Earth with mass  $3.58^{+0.25}_{-0.26} M_{\oplus}$  and radius  $1.70^{+0.18}_{-0.15} R_{\oplus}$  orbiting at a distance of  $\sim 0.02$  au from the host star, where it has  $T_{\text{eq}} \sim 1700$ – $1900$  K and photoevaporation would almost certainly have stripped any primordial H/He atmosphere (Kubyskhina et al. 2019). The third planet (HD 3167d) orbits at an intermediate distance of  $\sim 0.08$  au with a minimum mass of  $6.90 \pm 0.71 M_{\oplus}$  (Christiansen et al. 2017). Notably, radial velocity measurements made during primary transit indicate via the Rossiter–McLaughlin effect that HD 3167c is on an orbit crossing close to the stellar poles, suggestive of an active dynamical past

(Dalal et al. 2019) or a primordial misalignment of the stellar rotation axis (Bate et al. 2010; Batygin 2012; Christiansen et al. 2017). Measurements of the stellar  $H\alpha$  emission and Ca II H and K absorption also indicate that the host star is relatively quiescent (Gandolfi et al. 2017), enhancing the prospects for stable transmission spectroscopy measurements.

The paper is organized as follows. Section 2 describes the transit observations and data reduction, with light-curve fitting presented in Section 3. Host star elemental abundances derived from high-resolution spectra are reported in Section 4. The transmission spectrum of the planetary atmosphere and its implications are considered in Section 5. Models for the planetary interior structure are presented in Section 6. We discuss the results in a broader context in Section 7 and conclude in Section 8. We also note that a separate analysis of the HST WFC3 data is presented in a study by Guilluy et al., which we became aware of during the preparation of this manuscript.

## 2. Observations and Data Reduction

### 2.1. HST Spectroscopy

We observed five primary transits of HD 3167c with HST/WFC3 using the G141 grism, which covers a wavelength range of approximately 1.12–1.65  $\mu\text{m}$  with a spectral resolving power of  $R \sim 130$  at  $\lambda = 1.4 \mu\text{m}$ . The visits were made as part of GO-15333 (Crossfield & Kreidberg 2017b) on 2018 May 22, 2018 July 20, 2019 June 14, 2019 August 12, and 2020 July 5. We refer to these as the G141v1, G141v2, G141v3, G141v4, and G141v5 data sets, respectively. Observations for all visits consisted of seven HST orbits and were made using round-trip spatial scanning with a scan rate of  $0''.429 \text{ s}^{-1}$ . We adopted the SPARS25 sampling sequence with four nondestructive reads per exposure (NSAMP = 4), resulting in total integration times of 70 s and scans across approximately 240 pixel-rows of the cross-dispersion axis. For each science exposure, only the  $512 \times 512$  pixel subarray of the detector containing the target spectrum was read out. With this setup, we obtained 18 science exposures in the first HST orbit following acquisition and 20 exposures in each subsequent HST orbit. Typical peak frame counts were  $\sim 47,000$  electrons ( $e^-$ ) per pixel for all visits, which is within the recommended range derived from an ensemble analysis of WFC3 spatial-scan data spanning 8 yr (Stevenson & Fowler 2019). Spectra were extracted from the raw data frames using a custom-written Python code,<sup>27</sup> which has been described previously (Evans et al. 2016, 2017; Mikal-Evans et al. 2019). Further details are provided in Appendix A.

### 2.2. K2 and IRAC Photometry

Additional broadband transit measurements were made for HD 3167c at optical wavelengths with Kepler K2 (Howell et al. 2014) and at longer infrared wavelengths with Spitzer IRAC (Fazio 2004). Details of the K2 observations have previously been reported in Vanderburg et al. (2016), Christiansen et al. (2017), and Gandolfi et al. (2017). For the present study, we used the K2SFF photometry<sup>28</sup> (Vanderburg & Johnson 2014) available on the Mikulski Archive for Space Telescopes.<sup>29</sup> The single IRAC observation was made in the

4.5  $\mu\text{m}$  passband on 2016 October 31 as part of Program GO-13052 (Werner et al. 2016). Observations were performed in stare mode with exposure times of 0.4 s and lasted 11.5 hr, including a baseline of 3.8 hr before transit ingress and 2.8 hr after transit egress. Photometry was extracted using the custom-written Python code described in Evans et al. (2015) with a circular 3-pixel-radius aperture. Below we present a preliminary analysis of the resulting IRAC light curve to help constrain the HD 3167c transmission spectrum. However, a full analysis of this data set, along with additional IRAC transit observations for HD 3167b, will be presented in an upcoming study (K. K. Hardegree-Ullman et al. 2020, in preparation).

## 3. Light-curve Analysis

### 3.1. HST Broadband Light Curves

Broadband light curves were produced for all HST visits by summing each spectrum across the 0.8–1.95  $\mu\text{m}$  wavelength range. The resulting light curves are shown in Figures 1 and 2, exhibiting systematics typical of WFC3 transit data sets (e.g., Fraine et al. 2014; Knutson et al. 2014a; Kreidberg et al. 2014, 2020; Evans et al. 2016, 2017). We fit all five broadband light curves jointly, sharing the planet-to-star radius ratio ( $R_p/R_*$ ) across all light curves while allowing the transit midtimes ( $T_i$  for the  $i$ th data set) to vary separately for each data set. Other transit parameters were held fixed to the values listed in Table 1, namely, the normalized semimajor axis ( $a/R_*$ ), the orbital impact parameter ( $b$ ), period ( $P$ ), and eccentricity ( $e$ ); and quadratic stellar limb-darkening coefficients ( $u_1, u_2$ ). We also allowed the white noise to vary for each light curve, parameterized as a rescaling of the photon noise level ( $\beta_i$ ). Further details of our light-curve fitting methodology, including the sources of the values listed in Table 1 and the adopted transit and systematics models, are provided in Appendix B.

We marginalized the posterior distribution of the model parameters using the `emcee` Python package (Foreman-Mackey et al. 2013), which implements affine-invariant Markov Chain Monte Carlo (MCMC). The results are summarized in Table 1, with the best-fit models shown in Figures 2 and 3. For the transit depth we find  $(R_p/R_*)^2 = 852^{+45}_{-55}$  ppm, derived from the posterior sample values for  $R_p/R_* = 0.02919^{+0.00076}_{-0.00095}$ . Inferred values for the white-noise rescaling factors ( $\beta_1 = 1.90^{+0.17}_{-0.17}$ ,  $\beta_2 = 1.43^{+0.12}_{-0.10}$ ,  $\beta_3 = 1.68^{+0.15}_{-0.14}$ ,  $\beta_4 = 1.83^{+0.13}_{-0.14}$ ,  $\beta_5 = 1.48^{+0.11}_{-0.11}$ ) indicate that a high-frequency source of noise is affecting all data sets at a level of  $\sim 40\%$ – $90\%$  above the photon noise floor. This is evident in the broadband light-curve residuals shown in Figure 3.

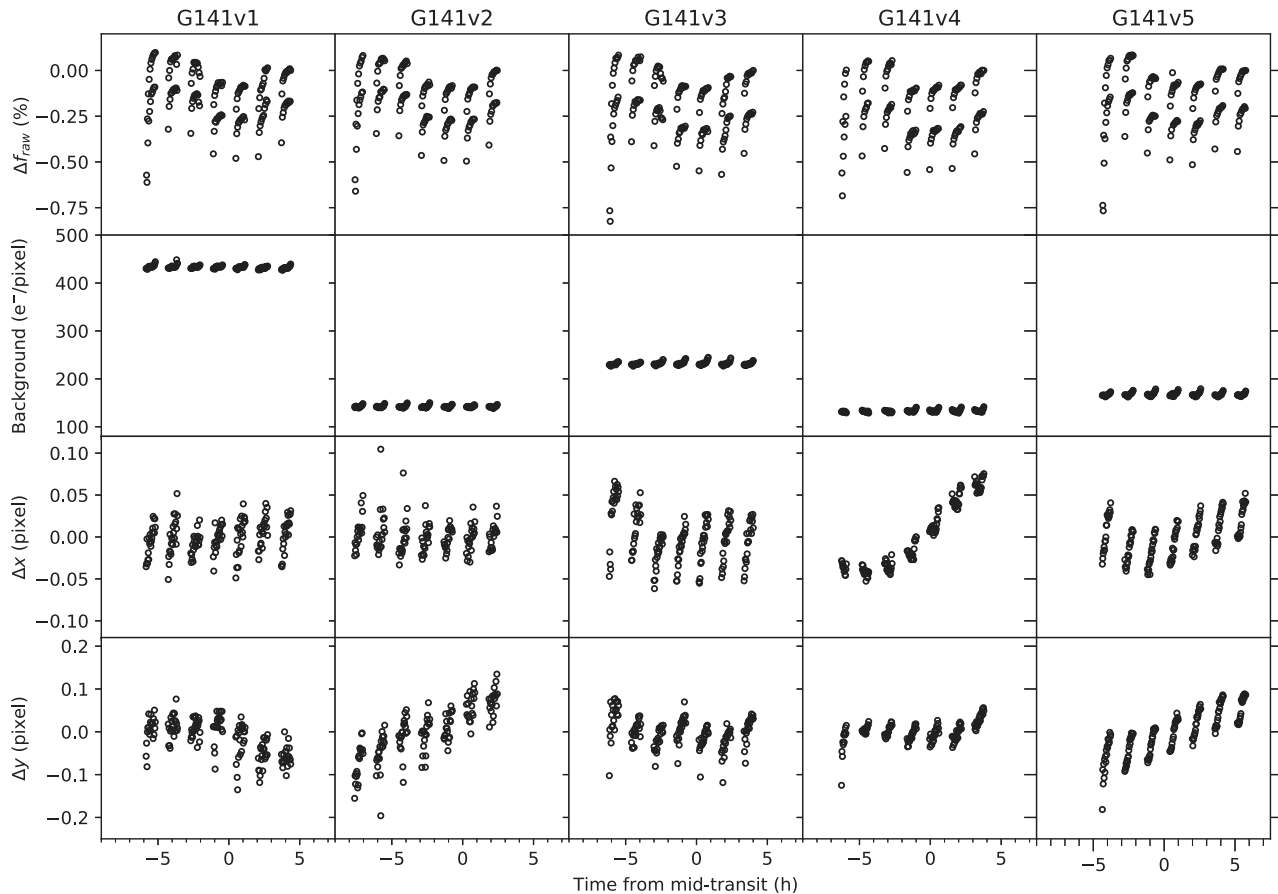
### 3.2. HST Spectroscopic Light Curves

Spectroscopic light curves were produced from the WFC3 data by summing flux within 28 equal-width channels between wavelengths 1.125 and 1.645  $\mu\text{m}$ . To do so, we followed a similar methodology to that used previously in Evans et al. (2016, 2017) and Mikal-Evans et al. (2019), which in turn was adapted from an original implementation by Deming et al. (2013). This involved first cross-correlating each 1D spectrum against a template spectrum, solving for both a lateral shift in wavelength and a wavelength-uniform rescaling of the flux. For our analysis, we adopted the final spectrum of each visit as the template spectrum. The residuals of this cross-correlation were

<sup>27</sup> <https://github.com/thommevans/wfc3>

<sup>28</sup> <https://archive.stsci.edu/prepds/k2sff/html/c08/ep220383386.html>

<sup>29</sup> <https://archive.stsci.edu>



**Figure 1.** Time series extracted from the spatial-scan images for each WFC3 visit. Rows from top to bottom are variation of the broadband relative flux ( $\Delta f_{\text{raw}}$ ), integrated background counts per pixel, median-subtracted drift along the dispersion axis ( $\Delta x$ ), and median-subtracted drift along the cross-dispersion axis ( $\Delta y$ ). Note the offset in  $f_{\text{raw}}$  between successive forward and backward exposures and the strong ramp systematics in the first HST orbit.

then binned in wavelength to produce a time series for each wavelength channel, before adding in the transit model derived from the broadband fit (Section 3.1) to produce the spectroscopic light curves.

In practice, this process is similar to other methods used in the literature for generating spectroscopic light curves from WFC3 data. Specifically, the flux rescaling step is equivalent to typical common-mode corrections, such as dividing the raw spectroscopic light curves by the broadband light curve (i.e.,  $f_{\text{raw}}$  shown in Figures 1 and 2). For example, Benneke et al. (2019b) produced spectroscopic light curves by dividing the binned fluxes through by the broadband time series. Accounting for the lateral shifts, denoted by  $\Delta x$  in Figure 1, helps to further minimize systematics in the spectroscopic light curves arising caused by pointing drift. For comparison, Benneke et al. (2019b) instead decorrelated against  $\Delta x$  during the light-curve fitting stage.

We fit the spectroscopic light curves following a similar approach to the broadband light-curve fits, with a few differences. In particular, we held the transit midtimes fixed to the best-fit values determined for the corresponding broadband light curve. Full details are given in Appendix C. Inferred values for  $R_p/R_*$  and the transit depth  $(R_p/R_*)^2$  are reported in Table 2. The median uncertainty for the inferred transit depths across all channels is 17 ppm, ranking among the most precise WFC3 transmission spectra published to date. Systematics-corrected spectroscopic light curves are shown in Figure 3. The median rms of the best-fit residuals is 150 ppm

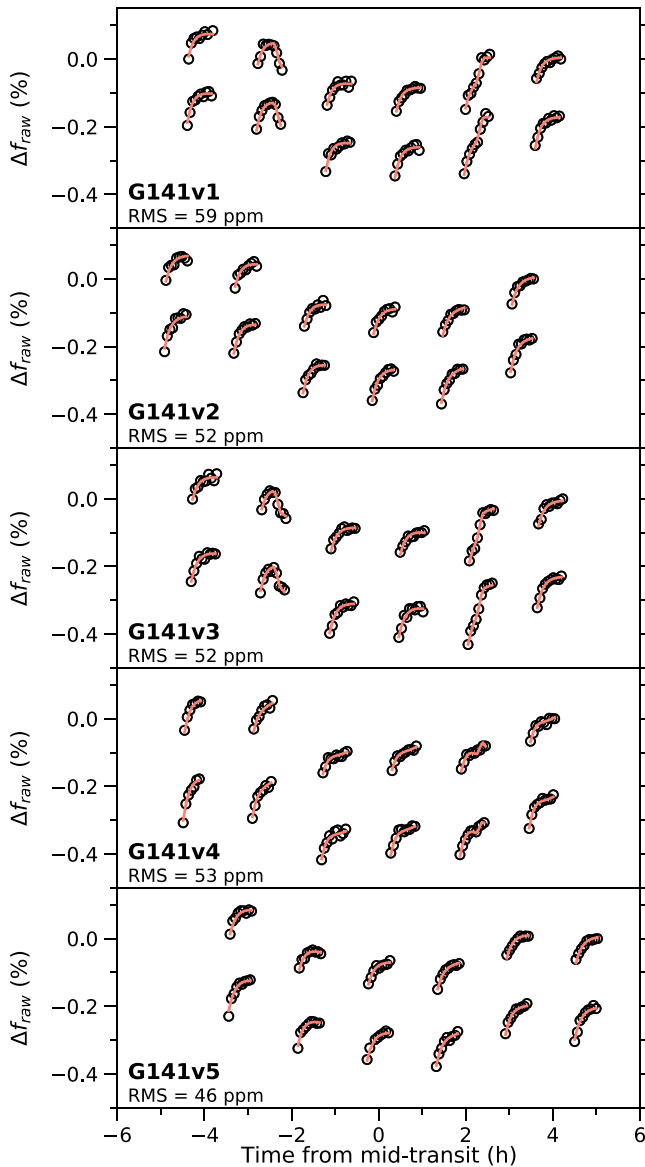
(per 70 s exposure), close to the median photon noise level of 138 ppm. Accordingly, the inferred white-noise rescaling factors are typically within  $\sim 10\%$  of unity across all spectroscopic channels (Figure 4). We also performed a second independent analysis using the data reduction and light-curve fitting code of Kreidberg et al. (2014). As described in Appendix D, this gave consistent results, increasing our confidence in the measured transmission spectrum.

### 3.3. K2 and IRAC Light Curves

Analysis of the K2 light curve followed largely the same approach described in Christiansen et al. (2017), but with two main differences. First, we fixed  $a/R_*$  and  $b$  to the same values used for the broadband WFC3 analysis (Table 1). Second, unlike Christiansen et al. (2017), we did not allow for secondary light dilution as a free parameter in our fit, as this could bias the measured  $R_p/R_*$  to larger values. This is justified by high-contrast imaging of the HD 3167 system, which confirms the lack of blending with nearby stars in the K2 photometry (see Appendix A for references). To fit the IRAC light curve, we used a Gaussian process (GP) approach similar to that employed for the HST broadband light curves. Details of the latter fit are provided in Appendix E.

## 4. Stellar Abundance Analysis

In addition to analyzing the transit light curves described in the previous sections, we used three spectra of HD 3167 to



**Figure 2.** Raw WFC3 broadband light curves with best-fit models. Data sets are labeled in the lower left corner of each axis with the rms of the model residuals. Note that the first HST orbit has been discarded for the light-curve fitting, as described in Appendix B.

conduct an assay of the stellar elemental abundances. These spectra were taken with Keck/HIRES (Vogt et al. 1994) on 2016 July 11 to provide the high signal-to-noise ratio stellar template used to calculate the precision radial velocities reported by Christiansen et al. (2017). The observations each exposed for 166 s using the B1 decker during good conditions and with an effective instrumental seeing of  $0''.9$ ; the spectra are publicly available from the Keck Observatory Archive.<sup>30</sup>

To measure the stellar abundances, we used the methodology and software tools of Brewer et al. (2016), to which readers may refer for a full description of these methods. In Table 3 we report the measured abundances for 15 elements, along with statistical and systematic uncertainties ( $\sigma_{\text{stat}}$  and  $\sigma_{\text{sys}}$ , respectively) for each. The  $\sigma_{\text{sys}}$  uncertainties come from Table 6 of Brewer et al. (2016) and essentially describe the reliability of the modeling code used to provide the same result for two

**Table 1**  
HD 3167c Properties

Parameter	Value	Note
$R_p/R_*$	$0.02919^{+0.00076}_{-0.00095}$	Free
$(R_p/R_*)^2$ (ppm)	$852^{+45}_{-55}$	Derived from $R_p/R_*$
$R_*$ ( $R_\odot$ )	$0.872 \pm 0.057$	Christiansen et al. (2017)
$R_p$ ( $R_\oplus$ )	$2.77^{+0.20}_{-0.20}$	Derived from $R_p/R_*$ and $R_*$
$u_1$	0.15 (fixed)	Fixed
$u_2$	0.31 (fixed)	Fixed
$P$ (days)	29.84622	Fixed
$e$	0	Fixed
$a/R_*$	45.9	Fixed
$b$	0.35	Fixed
$i$ ( $^\circ$ )	89.56	Derived from $R_*$ and $b$
$T_1$ (JD <sub>UTC</sub> )	$2458260.52959^{+0.00036}_{-0.00035}$	Free
$T_2$ (JD <sub>UTC</sub> )	$2458320.21401^{+0.00522}_{-0.00549}$	Free
$T_3$ (JD <sub>UTC</sub> )	$2458648.53174^{+0.00035}_{-0.00037}$	Free
$T_4$ (JD <sub>UTC</sub> )	$2458708.19273^{+0.00773}_{-0.00148}$	Free
$T_5$ (JD <sub>UTC</sub> )	$2459036.51367^{+0.00361}_{-0.00356}$	Free
$\beta_1$	$1.90^{+0.17}_{-0.17}$	Free
$\beta_2$	$1.43^{+0.12}_{-0.10}$	Free
$\beta_3$	$1.68^{+0.15}_{-0.14}$	Free
$\beta_4$	$1.83^{+0.13}_{-0.14}$	Free
$\beta_5$	$1.48^{+0.11}_{-0.11}$	Free

**Note.** Values with uncertainties correspond to MCMC posterior medians and 68% credible intervals for the WFC3 broadband light-curve analysis.

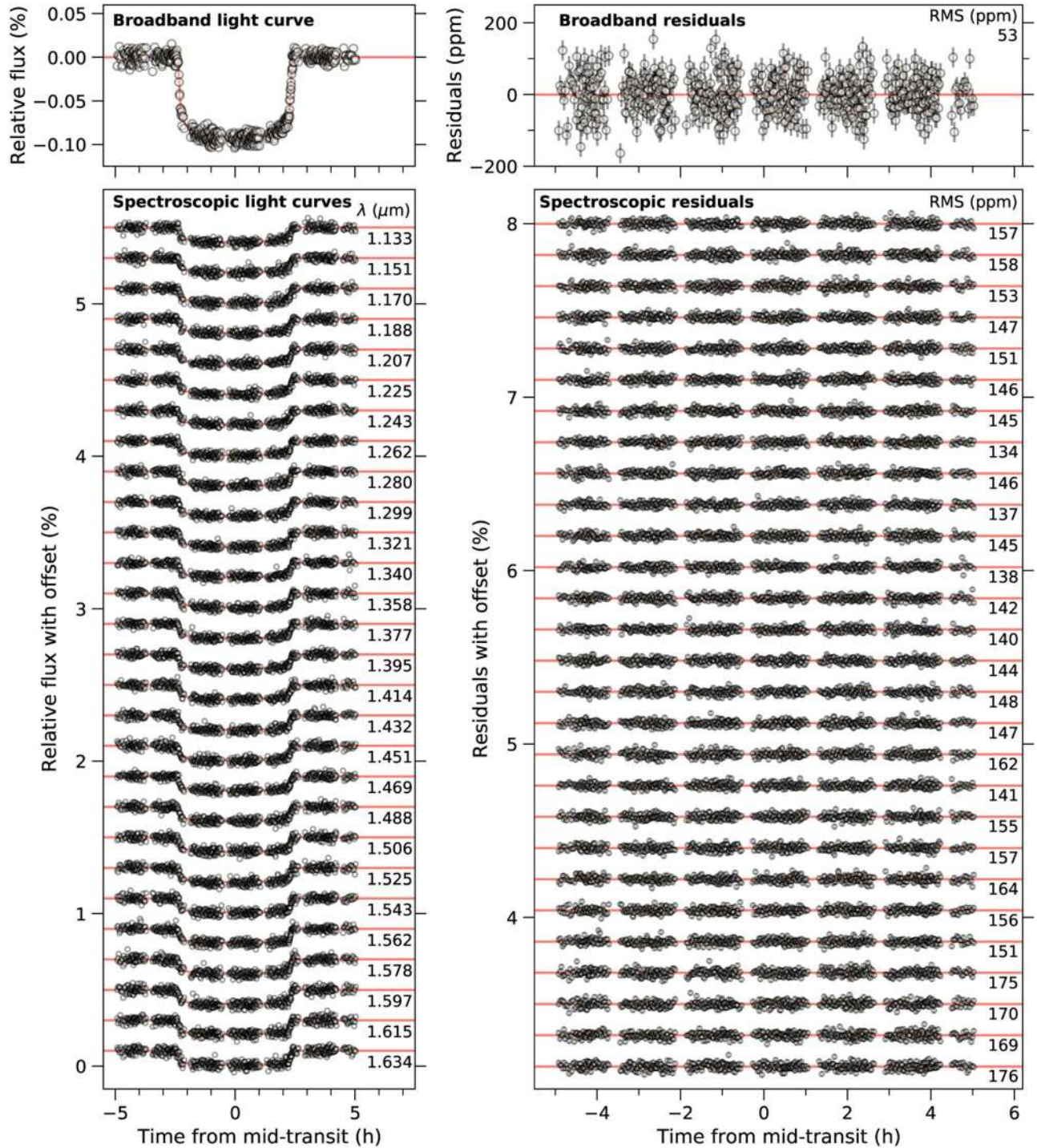
nearly identical spectra (not accounting for any additional uncertainty due to the star’s distance from solar values). The  $\sigma_{\text{stat}}$  values indicate the standard deviation on the abundances measured from each of the three HIRES spectra; these values are all smaller than  $\sigma_{\text{sys}}$ , likely because the three spectra were all taken on the same night.

The elemental abundance patterns seen in HD 3167 (Table 3) are similar to the solar values, with differences of  $<0.1$  dex for all 15 measured elements. In particular, our measurements indicate a stellar C/O = 0.48 and Mg/Si consistent with the solar value to within  $1\sigma$ , both entirely consistent with the peak of the distribution for local stars (Brewer & Fischer 2016). This suggests that models of planet formation, evolution, and atmospheres assuming solar abundances should be generally applicable to this system as well. We also find  $[Y/Mg] = -0.08 \pm 0.03$ , suggesting that the star may be slightly older than the Sun (consistent with earlier studies, e.g., Christiansen et al. 2017). Using the abundance–age relation of Nissen et al. (2020) and propagating all uncertainties using Monte Carlo techniques, we estimate a stellar age of  $6.7 \pm 0.8$  Gyr. This value should be interpreted cautiously, since HD 3167 is about 300 K cooler than the nearly solar-like stars used to calibrate that relation. However, it is in agreement with the age of  $7.8 \pm 4.3$  Gyr reported by Christiansen et al. (2017), which was determined by isochrone fitting.

## 5. Atmospheric Characterization

The measured transmission spectrum obtained from the light-curve fits presented in Sections 3.2 and 3.3 is shown in Figure 6. The K2 measurement constrains the broadband optical level at a precision of 15 ppm, comparable to that achieved for each of the individual WFC3 channels ( $\sim 17$  ppm;

<sup>30</sup> <https://koa.ipac.caltech.edu/>



**Figure 3.** Light-curve measurements for the combined HST WFC3 data set, after accounting for systematics, with best-fit transit signals. The top left panel shows the broadband light curve, and the top right panel shows the corresponding model residuals. Bottom panels show the same for the spectroscopic light curves.

Table 2). Note, however, that the overall WFC3 level is less well constrained to a precision of  $\sim 50$  ppm (Table 1), owing to the flexible GP approach we adopted for modeling the light-curve baseline level (Section 3.1). Relative to the K2 measurement, the IRAC level is also constrained relatively imprecisely ( $\sim 140$  ppm; Table 2), due to the presence of time-correlated noise in the light curve that was marginalized with a flexible GP (Figure 5). When comparing the data to models in Sections 5.1–5.3 below, we account for the uncertainty in

relative levels between the K2, WFC3, and IRAC data sets by allowing the overall WFC3 level to float as a free parameter.

The WFC3 data exhibit an apparent trough at around  $1.3 \mu\text{m}$ . The depth of this feature is  $\sim 30$ – $50$  ppm, corresponding to a variation of approximately 3–5 atmospheric pressure scale heights, in line with expectations for molecular absorption bands at near-infrared wavelengths. This calculation was made by taking the equilibrium temperature ( $T_{\text{eq}} \sim 500$ – $600$  K) and surface gravity ( $g \approx 10.7 \text{ m s}^{-2}$ ) of HD 3167c and assuming an atmospheric mean molecular weight of  $\mu_{\text{atm}} = 5$  atomic

**Table 2**  
Similar to Table 1, for the WFC3 Spectroscopic Light-curve Fits of Our Primary Analysis, and the K2 and IRAC Analyses

Data Set	$\lambda$ ( $\mu\text{m}$ )	$R_p/R_*$	$(R_p/R_*)^2$ (ppm)	$u_1$ (fixed)	$u_2$ (fixed)
K2	0.45–0.65	0.03005 <sup>+0.00025</sup> <sub>-0.00025</sub>	903 <sup>+15</sup> <sub>-15</sub>	0.490	0.194
WFC3	1.125–1.144	0.02960 <sup>+0.00029</sup> <sub>-0.00028</sub>	879 <sup>+19</sup> <sub>-18</sub>	0.244	0.247
	1.144–1.162	0.02936 <sup>+0.00027</sup> <sub>-0.00024</sub>	863 <sup>+18</sup> <sub>-16</sub>	0.243	0.249
	1.162–1.181	0.02940 <sup>+0.00026</sup> <sub>-0.00025</sub>	866 <sup>+17</sup> <sub>-16</sub>	0.233	0.255
	1.181–1.199	0.02919 <sup>+0.00028</sup> <sub>-0.00029</sub>	852 <sup>+18</sup> <sub>-18</sub>	0.230	0.255
	1.199–1.218	0.02898 <sup>+0.00029</sup> <sub>-0.00027</sub>	838 <sup>+18</sup> <sub>-17</sub>	0.225	0.259
	1.218–1.236	0.02917 <sup>+0.00026</sup> <sub>-0.00028</sub>	851 <sup>+17</sup> <sub>-18</sub>	0.220	0.266
	1.236–1.255	0.02874 <sup>+0.00024</sup> <sub>-0.00026</sub>	823 <sup>+15</sup> <sub>-17</sub>	0.215	0.269
	1.255–1.273	0.02935 <sup>+0.00024</sup> <sub>-0.00026</sub>	862 <sup>+16</sup> <sub>-16</sub>	0.208	0.275
	1.273–1.292	0.02898 <sup>+0.00026</sup> <sub>-0.00025</sub>	839 <sup>+17</sup> <sub>-16</sub>	0.187	0.290
	1.292–1.310	0.02888 <sup>+0.00024</sup> <sub>-0.00027</sub>	832 <sup>+15</sup> <sub>-17</sub>	0.197	0.285
	1.310–1.329	0.02917 <sup>+0.00026</sup> <sub>-0.00025</sub>	851 <sup>+16</sup> <sub>-16</sub>	0.189	0.289
	1.329–1.347	0.02884 <sup>+0.00025</sup> <sub>-0.00023</sub>	830 <sup>+16</sup> <sub>-15</sub>	0.182	0.296
	1.347–1.366	0.02928 <sup>+0.00021</sup> <sub>-0.00023</sub>	858 <sup>+14</sup> <sub>-15</sub>	0.175	0.302
	1.366–1.384	0.02935 <sup>+0.00027</sup> <sub>-0.00025</sub>	862 <sup>+18</sup> <sub>-16</sub>	0.165	0.310
	1.384–1.403	0.02961 <sup>+0.00024</sup> <sub>-0.00023</sub>	879 <sup>+15</sup> <sub>-15</sub>	0.158	0.317
	1.403–1.421	0.02945 <sup>+0.00027</sup> <sub>-0.00025</sub>	869 <sup>+17</sup> <sub>-16</sub>	0.149	0.323
	1.421–1.440	0.02983 <sup>+0.00024</sup> <sub>-0.00023</sub>	894 <sup>+16</sup> <sub>-15</sub>	0.141	0.328
	1.440–1.458	0.02987 <sup>+0.00027</sup> <sub>-0.00025</sub>	896 <sup>+18</sup> <sub>-17</sub>	0.130	0.335
	1.458–1.477	0.02921 <sup>+0.00022</sup> <sub>-0.00023</sub>	853 <sup>+14</sup> <sub>-15</sub>	0.121	0.344
	1.477–1.495	0.02926 <sup>+0.00028</sup> <sub>-0.00027</sub>	856 <sup>+18</sup> <sub>-16</sub>	0.112	0.348
	1.495–1.514	0.02900 <sup>+0.00027</sup> <sub>-0.00026</sub>	840 <sup>+17</sup> <sub>-17</sub>	0.105	0.348
	1.514–1.532	0.02961 <sup>+0.00027</sup> <sub>-0.00025</sub>	879 <sup>+18</sup> <sub>-16</sub>	0.092	0.361
	1.532–1.551	0.02937 <sup>+0.00029</sup> <sub>-0.00029</sub>	864 <sup>+19</sup> <sub>-19</sub>	0.080	0.368
	1.551–1.569	0.02923 <sup>+0.00025</sup> <sub>-0.00025</sub>	855 <sup>+16</sup> <sub>-16</sub>	0.075	0.367
	1.569–1.588	0.02972 <sup>+0.00033</sup> <sub>-0.00030</sub>	886 <sup>+22</sup> <sub>-20</sub>	0.070	0.363
	1.588–1.606	0.02972 <sup>+0.00031</sup> <sub>-0.00026</sub>	887 <sup>+20</sup> <sub>-17</sub>	0.066	0.365
	1.606–1.625	0.02880 <sup>+0.00031</sup> <sub>-0.00029</sub>	827 <sup>+20</sup> <sub>-18</sub>	0.055	0.368
	1.625–1.643	0.02934 <sup>+0.00028</sup> <sub>-0.00032</sub>	861 <sup>+18</sup> <sub>-20</sub>	0.052	0.368
IRAC2	4–5	0.02983 <sup>+0.00233</sup> <sub>-0.00238</sub>	890 <sup>+139</sup> <sub>-142</sub>	0.042	0.129

**Table 3**  
HD 3167 Host Star Element Abundances

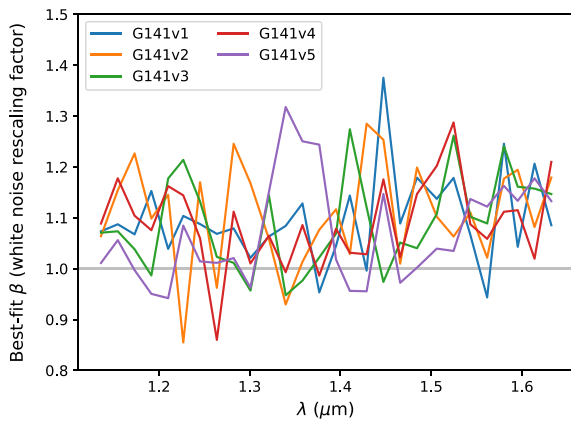
Abundance	Value	$\sigma_{\text{stat}}$	$\sigma_{\text{sys}}$
[C/H]	0.01	0.003	0.026
[N/H]	−0.03	0.013	0.042
[O/H]	0.07	0.008	0.036
[Na/H]	0.05	0.002	0.014
[Mg/H]	0.06	0.004	0.012
[Al/H]	0.08	0.006	0.028
[Si/H]	0.07	0.003	0.008
[Ca/H]	0.05	0.001	0.014
[Ti/H]	0.07	0.002	0.012
[V/H]	0.07	0.005	0.034
[Cr/H]	0.04	0.003	0.014
[Mn/H]	0.03	0.001	0.020
[Fe/H]	0.04	0.000	0.010
[Ni/H]	0.05	0.002	0.012
[Y/H]	−0.02	0.005	0.030

### 5.1. Equilibrium Chemistry Forward Models

Model transmission spectra were generated under the assumption that the atmosphere is in both chemical and radiative equilibrium, following the same approach outlined in Benneke (2015) and Benneke et al. (2019a). To do this, we treated the atmosphere as being one-dimensional (1D) and considered various levels of heavy-element enrichment, ranging from 1 to 1000 $\times$  solar metallicity. The Bond albedo was set to 30%, with heat redistribution from the dayside to nightside hemispheres assumed to be uniform. We then iteratively solved for chemical and radiative–convective equilibrium to obtain a self-consistent solution for the 1D globally averaged chemical composition and pressure–temperature (PT) profile for each metal enrichment.

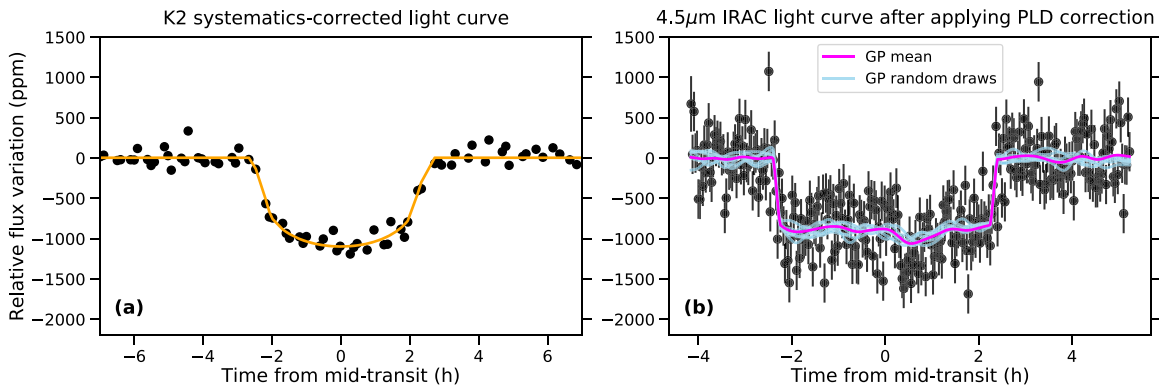
The resulting model transmission spectra are shown in Figure 6, with corresponding PT profiles in Figure 7. We find that good agreement is obtained with the data for those models with metallicity  $\gtrsim 300\times$  solar. Specifically, we obtain reduced  $\chi^2$  values close to unity for the 700 $\times$  solar ( $\chi^2 = 1.2$ ) and 1000 $\times$  solar ( $\chi^2 = 1.1$ ) cases. By contrast, the data are marginally inconsistent with the 300 $\times$  solar model at the  $2.3\sigma$  level of significance. The discrepancy increases to  $>5\sigma$  for all models with metallicity  $\leq 100\times$  solar.

However, we note three important caveats. First, all models shown in Figure 6 assume a carbon-to-oxygen ratio (C/O) equal to the solar value of C/O = 0.54 (Asplund et al. 2009), broadly consistent with what we measured for HD 3167 (Table 3). Nonetheless, a C/O ratio differing from that of the host star is plausible, depending on where in the protoplanetary disk HD 3167c formed and the composition of material it subsequently accreted (Öberg et al. 2011). Second, we have ignored the effect of clouds, which can be highly degenerate with atmospheric metallicity at the level of our data precision (Benneke & Seager 2013). Third, we adopted a globally averaged self-consistent 1D solution for the PT profile given an assumed albedo. While it has been shown that global-average temperature profiles provide a reasonable approximation to temperature profiles at the planetary limb (e.g., Fortney et al. 2010), the overall temperature will still depend on the unknown albedo. In the next section, we investigate these effects further by performing a retrieval analysis that includes clouds and



**Figure 4.** Best-fit white-noise rescaling factors ( $\beta$ ) inferred for each spectroscopic light curve.

mass units (amu). The latter is consistent with sub-Neptune population synthesis simulations (e.g., Fortney et al. 2013), although there is anticipated to be a large spread due to the stochastic nature of planetesimal accretion during formation. In the following sections, we compare the data with detailed models of the planetary atmosphere.



**Figure 5.** (a) Systematics-corrected K2 light curve with best-fit transit model. (b) IRAC light curve after applying the PLD correction described in the text. Residual correlations with a characteristic amplitude of  $\sim 100$  ppm remain visible in the data, motivating the use of a  $t$ -dependent GP in the systematics modeling. The purple line shows the best-fit transit signal multiplied by the GP mean function, and light-blue lines show random draws from the GP.

allows the atmospheric metallicity, C/O ratio, and temperature to vary.

## 5.2. Retrieval Analysis with Chemically Consistent Atmosphere Models

To investigate a broader range of atmospheric properties for HD 3167c, we performed a retrieval analysis using the SCARLET retrieval framework (e.g., Benneke & Seager 2012, 2013; Knutson et al. 2014a; Kreidberg et al. 2014; Benneke 2015; Benneke et al. 2019a, 2019b; Wong et al. 2020). For the analysis in this section, we employed the chemically consistent mode of SCARLET described in Benneke (2015), which considers the space of models satisfying thermochemical equilibrium. We assumed an isothermal PT profile and allowed the temperature ( $T_{\text{atm}}$ ) to vary as a free parameter, along with the metallicity ( $[M/H]$ ), C/O, and a gray cloud-top pressure ( $P_c$ ). We adopted a uniform prior for  $T_{\text{atm}} \sim \mathcal{U}(400, 800)$  K, a log-uniform prior for  $[M/H] \sim \log \mathcal{U}(-2, 4)$  (dex), and a log-uniform prior for  $P_c \sim \log \mathcal{U}(-8, 2)$  (dex bar). For C/O, we applied a broad uniform prior on a custom-stretched parameter space, designed to provide the most effective sampling of the parameter space, as described in Benneke (2015). We then marginalized over the parameter space using nested sampling (Skilling 2004) with 10,000 active samples. The resulting parameter posterior distributions are shown in Figure 8. The credible distribution of model transmission spectra and highest likelihood model are shown in Figure 9, providing a good match to the data within the uncertainties.

Allowing for the presence of cloud in this manner, we are unable to place a strong constraint on the atmospheric metallicity. As has been discussed extensively elsewhere (e.g., Benneke & Seager 2013), the effects on the transmission spectrum of varying gas species abundances and the pressure level of a gray cloud deck can be effectively indistinguishable. A close-up view of this degeneracy is shown in Figure 10, with metallicities ranging from subsolar to  $1000\times$  solar allowed by the data, depending on the unknown role played by clouds. In addition, we are unable to place a meaningful constraint on the C/O ratio. However, this is not surprising, as to do so would require both carbon-bearing and oxygen-bearing species to be resolved by the data. As we explore in the next section, the available data are unable to confidently discriminate between major gases expected at the wavelengths covered by the data, such as  $\text{H}_2\text{O}$ ,  $\text{CH}_4$ , and  $\text{CO}_2$ .

## 5.3. Retrieval Analyses with Free Chemistry

In this section, we describe “free chemistry” retrieval analyses for which chemical equilibrium was not imposed. Instead, the abundances of individual gas species were allowed to vary without constraint. This was done using two independent codes: SCARLET (Benneke & Seager 2012, 2013) and petitRADTRANS (Mollière et al. 2019).

### 5.3.1. SCARLET Free Chemistry Retrievals

The SCARLET free chemistry retrievals proceeded in a similar manner to those described for the equilibrium chemistry retrievals described in Section 5.2, with a number of important differences. In particular, the mole fractions of individual gas species are included as free parameters of the model, rather than  $[M/H]$  and C/O. The spectrally active gas species we considered in this manner were  $\text{H}_2\text{O}$ ,  $\text{CH}_4$ ,  $\text{CO}$ ,  $\text{CO}_2$ ,  $\text{NH}_3$ , and  $\text{HCN}$ . We also included the mole fraction of  $\text{N}_2$  as a free parameter, despite it not having spectral features at the wavelengths covered by our data set. Nonetheless,  $\text{N}_2$  is predicted to be abundant in the atmosphere of HD 3167c (Section 5.4) and can affect the atmospheric pressure scale height, and thus the amplitude of spectral features. Aside from these gases, we assumed that the rest of the atmosphere was composed of H/He in solar proportions. For the mole fractions of the free gases, we employed log-uniform priors between  $10^{-10}$  and 1. As for the chemical equilibrium retrievals, we assumed an isothermal PT profile and allowed  $T_{\text{atm}}$  to vary as a free parameter, along with the pressure level of a gray cloud deck ( $P_c$ ), and adopted the same priors described in Section 5.2.

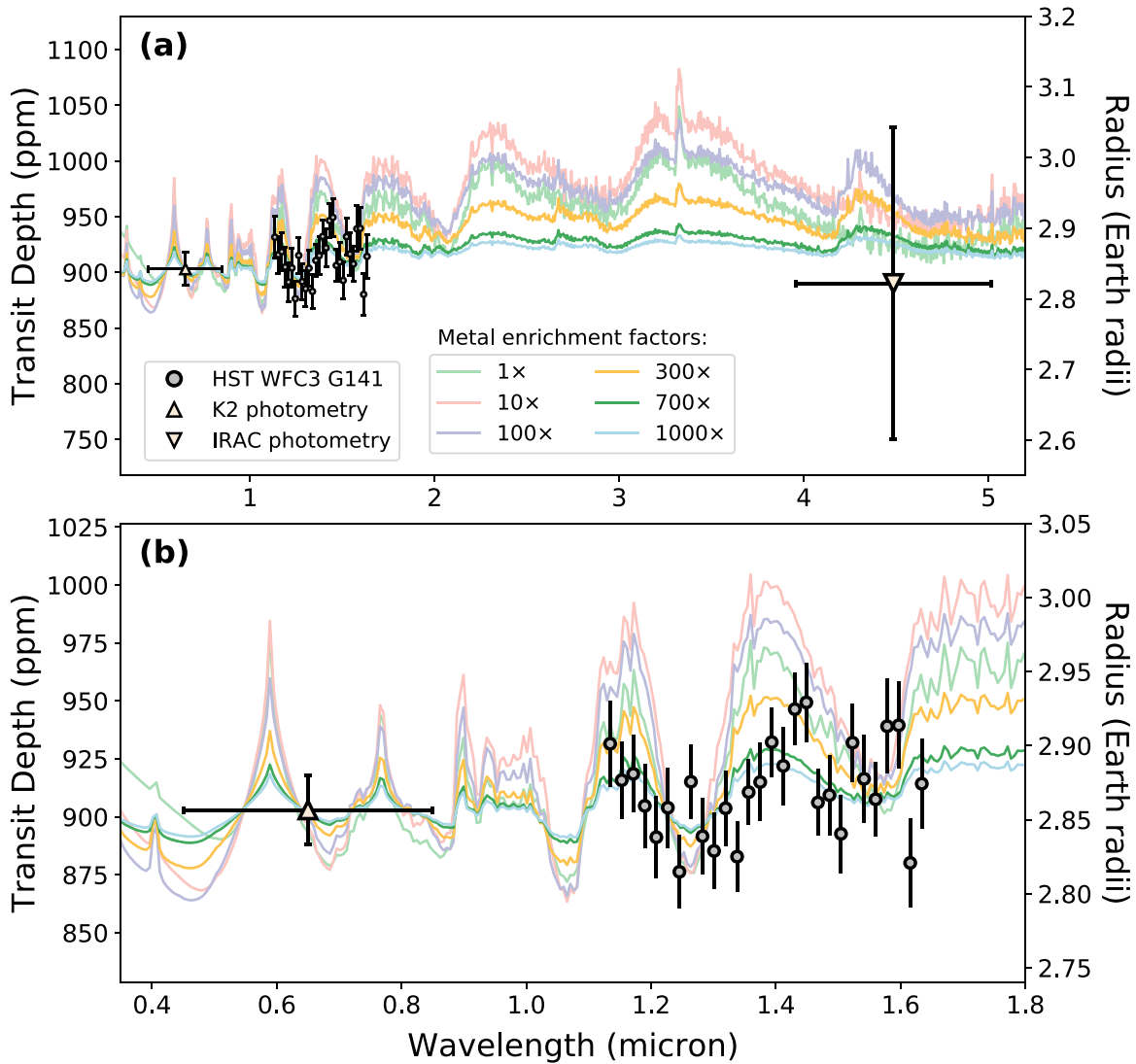
### 5.3.2. petitRADTRANS Free Chemistry Retrievals

A second free chemistry retrieval was conducted using the publicly available<sup>31</sup> petitRADTRANS (pRT) Python package (Mollière et al. 2019), in a manner similar to the SCARLET analysis described in the previous section. Specifically, we used pRT to take atmospheric properties as input and return model transmission spectra as output. This allowed us to define a log-likelihood function and marginalize over the model parameter space using multimodal nested sampling, as implemented by the publicly available<sup>32</sup> PyMultiNest package (Buchner et al. 2014). As for the SCARLET analysis, we allowed the

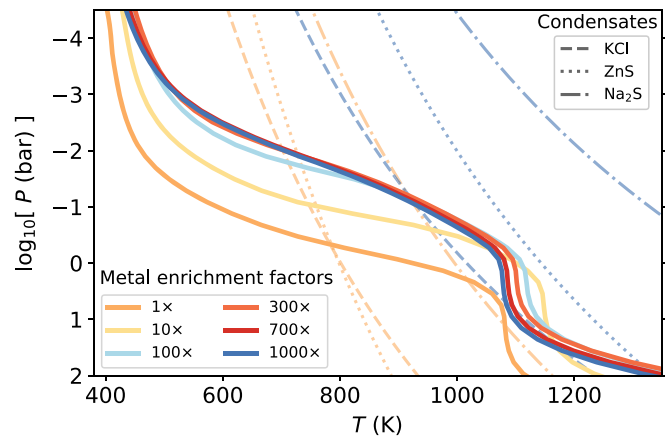
<sup>31</sup> <https://petitradtrans.readthedocs.io>

<sup>32</sup> <https://johannesbuchner.github.io/PyMultiNest>





**Figure 6.** (a) Transmission spectrum for HD 3167c measured with K2, HST, and Spitzer. Colored lines show chemical equilibrium models for different heavy-element enrichments relative to solar abundances. Note that a small offset has been applied to the HST data relative to the K2 and IRAC, within the uncertainty of the broadband level. (b) Same as panel (a), but covering a narrower wavelength range centered on the K2 and HST data.



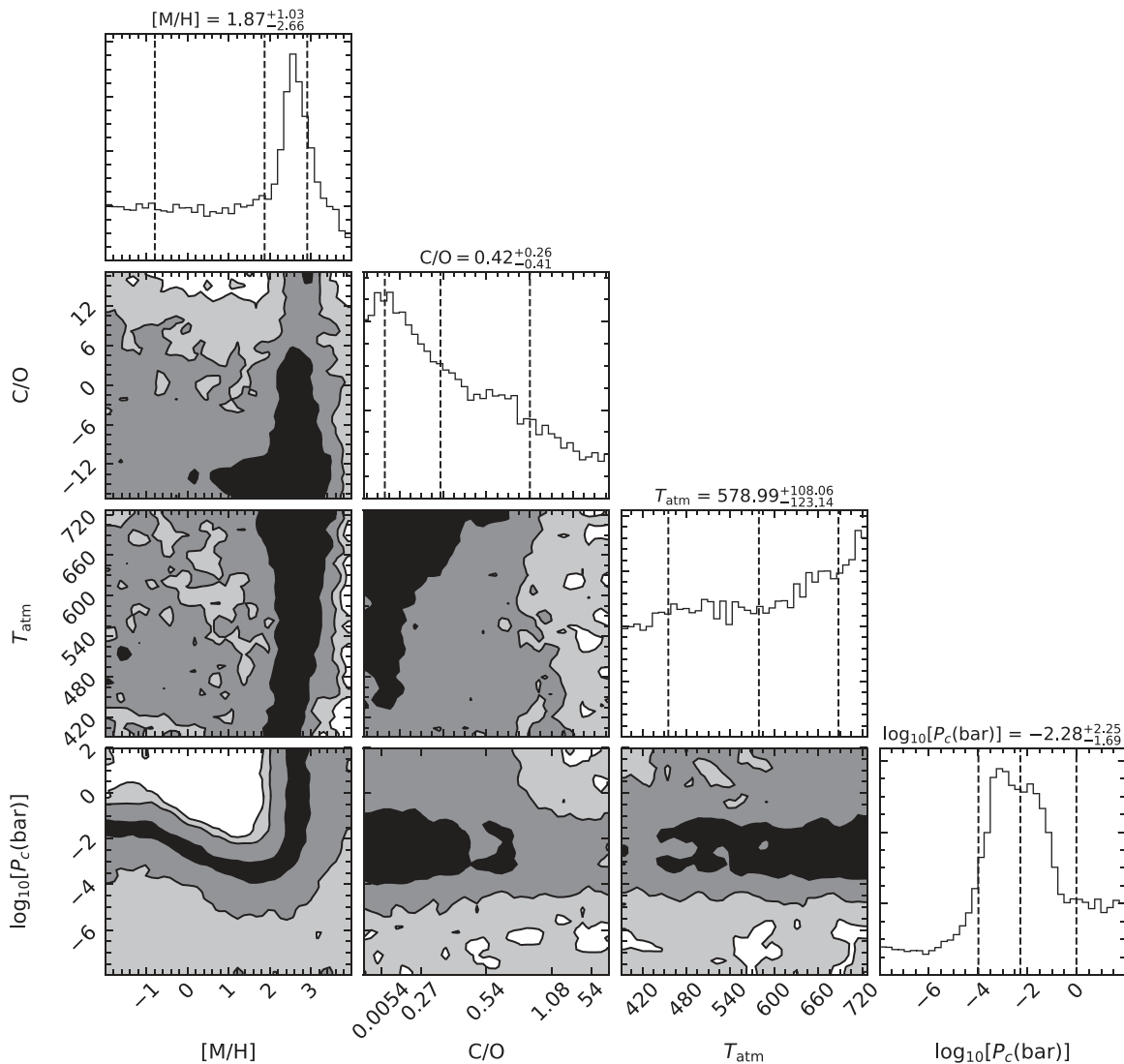
**Figure 7.** Thick solid lines show pressure–temperature profiles derived self-consistently for a selection of atmospheric metallicities, assuming chemical equilibrium. Condensation curves are shown for KCl (dashed lines), ZnS (dotted lines), and Na<sub>2</sub>S (dotted–dashed lines) for 1× and 1000× solar metallicity, using the same color scheme. Condensation curves for intermediate metallicities fall between these two end cases. Note that the condensation curve for H<sub>2</sub>O is to the left of the axis.

mole fractions of H<sub>2</sub>O, CH<sub>4</sub>, CO, CO<sub>2</sub>, NH<sub>3</sub>, HCN, and N<sub>2</sub> to vary with log-uniform priors between 10<sup>-10</sup> and 1. Again,  $T_{\text{atm}}$  and  $P_c$  were included as additional free parameters with the same priors assumed for the SCARLET retrievals.

### 5.3.3. Free Chemistry Retrieval Results

The posterior distributions for the SCARLET and *petitRADTRANS* free chemistry retrievals are shown in Figures 11 and 12, respectively, and summarized in Table 4. The results of both retrieval analyses are in broad agreement for most parameters, but there is some tension for the retrieved abundances of HCN and CO<sub>2</sub>. The SCARLET retrieval favors a higher HCN abundance relative to the *petitRADTRANS* retrieval, while the opposite is true for the inferred CO<sub>2</sub> abundances. However, in all cases the posteriors are broad, with the 1 $\sigma$  credible ranges of both retrievals overlapping for HCN and CO<sub>2</sub>.

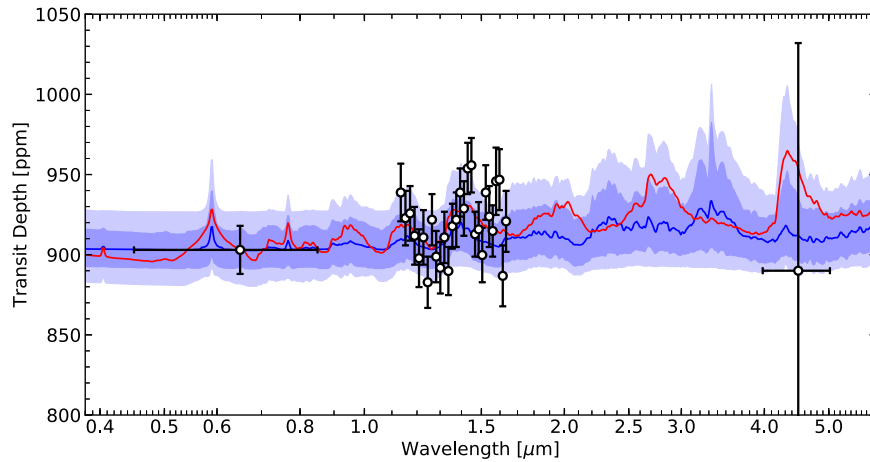
The posterior distributions reported in Table 4 provide the plausible mole fractions for each gas species that would be consistent with the measured transmission spectrum. Alone, however, they do not allow us to assess the evidence for any



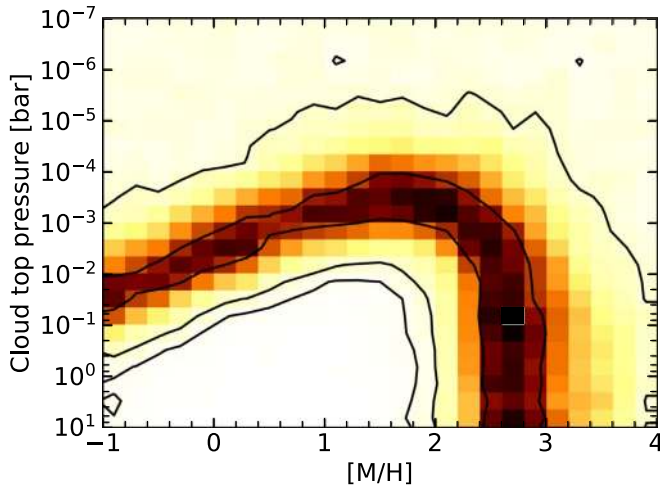
**Figure 8.** Posterior distributions inferred for free parameters of the chemically consistent SCARLET model: metallicity ( $[M/H]$ ), carbon-to-oxygen ratio ( $C/O$ ), and atmospheric temperature ( $T_{\text{atm}}$ ). Diagonal panels show the fully marginalized distribution for each parameter, with vertical dashed lines showing the median and  $1\sigma$  credible ranges. Off-diagonal panels show the marginalized posterior distributions for each pair of model parameters. Contours and shading indicate the  $1\sigma$ ,  $2\sigma$ , and  $3\sigma$  credible regions.

particular gas species actually being present in the atmosphere. To address this separate question, we employed the Bayesian model comparison framework outlined in Benneke & Seager (2013). This involved systematically excluding one or more gas absorbers from the model and repeating the SCARLET and petitRADTRANS retrieval analyses. Each time, the Bayesian evidence  $\mathcal{Z}$  of the resulting model would be recorded, as returned by the nested sampling algorithm. Denoting the evidence of the model with all gas absorbers included as  $\mathcal{Z}_0$ , the Bayes factor was then computed as  $B = \mathcal{Z}_0/\mathcal{Z}$ . Under this formulation,  $B$  can be considered the likelihood ratio of the removed absorber being present in the atmosphere. This can also be expressed as an equivalent “ $N$  sigma” ( $N_\sigma$ ) statistical significance under the frequentist paradigm using the approach described in Trotta (2008). The results of this analysis are given in Table 5. Neither retrieval uncovers even tentative ( $>2\sigma$ ) evidence for an individual gas absorber. Therefore, we cannot claim the unambiguous detection of any specific gas species based on the available data.

As reported in Table 5, we also investigated removing two or three gas species at a time and computing the resulting Bayes factors. This approach was motivated by the reasonable expectation that multiple gas absorbers are likely to be present in the atmosphere, rather than a single spectrally active gas. Although the absorption signature of any individual gas may not be statistically significant, the combined signature of multiple gases may be. Indeed, when  $\text{H}_2\text{O}$ ,  $\text{CH}_4$ , and  $\text{HCN}$  are removed from the model, the resulting Bayes factors imply positive evidence at  $2.7\sigma$  significance for the SCARLET analysis and  $2.2\sigma$  significance for the petitRADTRANS analysis. As listed in Table 5, a number of additional molecule combinations were tested with petitRADTRANS, which showed levels of evidence intermediate to these values, namely, the combinations  $\text{H}_2\text{O}+\text{CH}_4$  ( $2.4\sigma$ ),  $\text{H}_2\text{O}+\text{CO}_2$  ( $2.4\sigma$ ),  $\text{H}_2\text{O}+\text{HCN}$  ( $2.4\sigma$ ),  $\text{H}_2\text{O}+\text{CO}_2+\text{CH}_4$  ( $2.5\sigma$ ), and  $\text{H}_2\text{O}+\text{CO}_2+\text{HCN}$  ( $2.5\sigma$ ). From these results, we determine that molecular absorption is detected in the transmission spectrum at  $\sim 2.5\sigma$  significance, likely due to one or more of  $\text{H}_2\text{O}$ ,  $\text{CH}_4$ ,  $\text{CO}_2$ , and  $\text{HCN}$ .



**Figure 9.** Measured transmission spectrum for HD 3167c compared with model spectra obtained from the chemically consistent SCARLET retrieval analysis. The blue line gives the median of all posterior samples, with blue shading indicating  $1\sigma$  and  $2\sigma$  credible intervals. The red line shows the model spectrum corresponding to the highest likelihood sample.



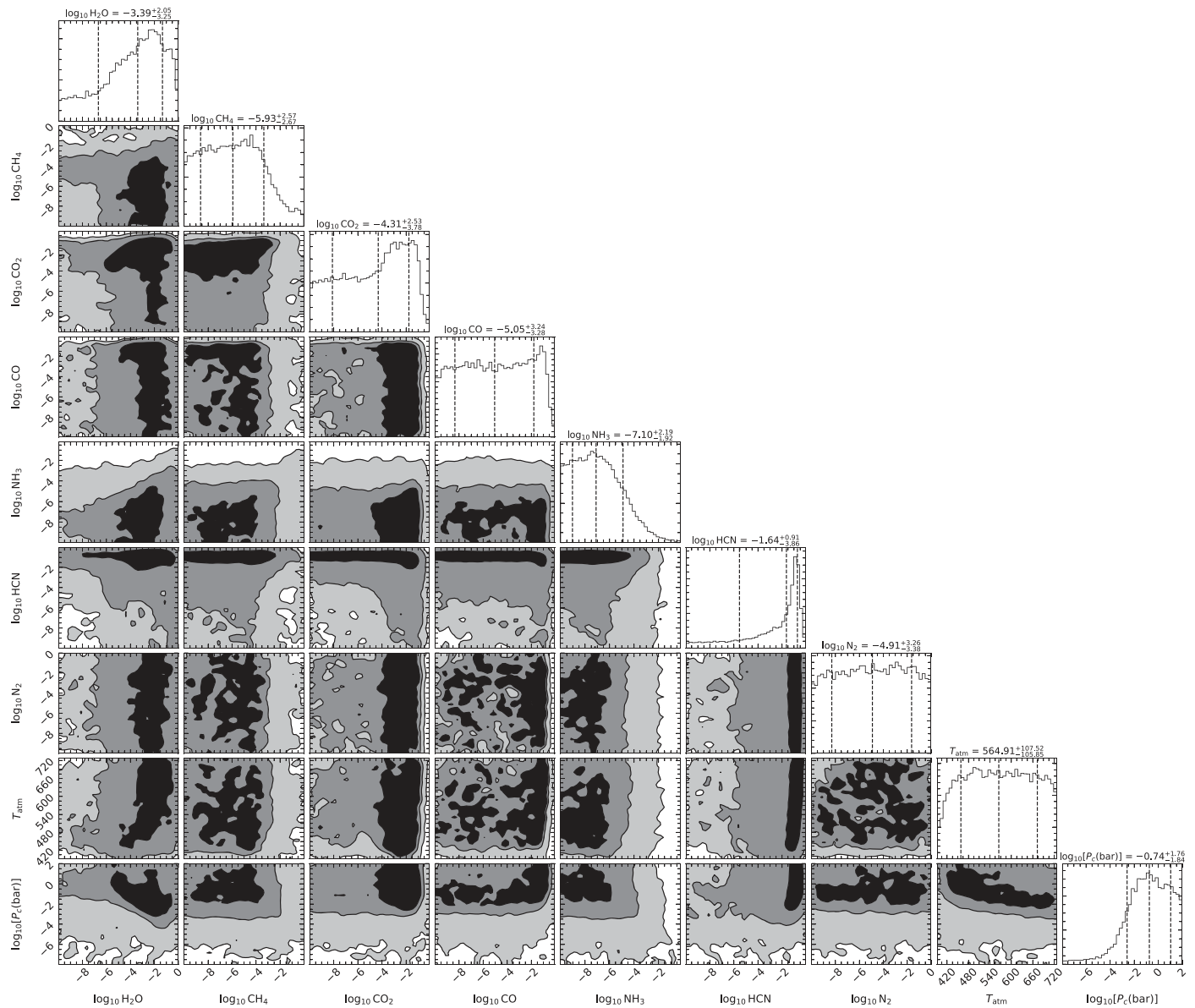
**Figure 10.** Joint constraints on the metallicity vs. the cloud-top pressure inferred by the chemically consistent SCARLET retrieval. Colored shading indicates the normalized probability density as a function of water abundance above the clouds and cloud-top pressure. Black contours show the  $1\sigma$ ,  $2\sigma$ , and  $3\sigma$  credible regions.

#### 5.4. Self-consistent Models with Disequilibrium Chemistry

To investigate the influence of disequilibrium chemistry on plausible atmospheric compositions for HD 3167c, we ran the thermochemical–photochemical kinetics and transport code described in Moses et al. (2013). This code accounts for vertical mixing, as well as photochemistry resulting from incident UV photons from the host star. For the latter, we assumed a UV spectrum corresponding to solar-cycle average conditions, taken from Woods & Rottman (2002). For the vertical mixing, we assumed an eddy diffusion coefficient of  $K_{zz} = 2 \times 10^9 \text{ cm}^2 \text{ s}^{-2}$  in the deep convective region of the atmosphere. At lower pressures ( $<500$  bar), we adopted a relation of the form  $K_{zz} = \eta(1 \text{ bar}/P)^{0.65} \text{ cm}^2 \text{ s}^{-2}$ , based on work by Parmentier et al. (2013) and Agúndez et al. (2014) tracking passive tracer particles in 3D general circulation models. We set  $\eta = 5 \times 10^6$ , which is lower than the values recommended in the latter studies for hot Jupiters, but likely more appropriate for the lower temperature of HD 3167c (e.g., Komacek et al. 2019). To restrict the eddy diffusion coefficient to reasonable values at high altitudes, an upper limit of

$K_{zz} = 2 \times 10^{10} \text{ cm}^2 \text{ s}^{-2}$  was imposed. The models were run for a range of heavy-element enrichments ranging from 100 to  $1000\times$  solar and C/O values of 0.2, 0.54 (i.e., solar), and 0.9. For each metallicity, we adopt the PT profiles computed in Section 5.1 under the assumption of chemical equilibrium.

The resulting pressure-dependent chemical abundances are shown in Figure 13. At the pressures probed by the transmission spectrum (between approximately  $10^{-1}$  and  $10^{-4}$  bar), the predicted mole fractions are broadly consistent with the abundance constraints derived from the free chemistry retrievals (Table 4). Admittedly, this is primarily due to the latter being poorly constrained, making them compatible with a large range of atmospheric conditions. Nonetheless, we venture to make a few observations. First, the self-consistent models presented in this section predict the HCN abundance to not exceed  $\sim 300$  ppm. Thus, the peak exhibited by the SCARLET posterior distribution for HCN mole fractions  $>1\%$  (Figure 11) seems unlikely from a physical perspective. Instead, we expect the true HCN mole fraction to be contained within the broad lower tail of the SCARLET posterior distribution, which extends down below the 1 ppm level. Meanwhile, as noted above in Section 5.3.3, the petitRADTRANS posterior distribution shows an analogous peak around relatively high ( $>1000$  ppm) mole fractions for  $\text{CO}_2$ , rather than HCN. As has been noted previously (e.g., Moses et al. 2013; Moses 2014), the  $\text{CO}_2$  abundance is highly sensitive to the overall metallicity of the atmosphere. This is clearly evident in Figure 13, with  $\text{CO}_2$  mole fractions increasing from  $<1\%$  for  $100\times$  solar metallicity to nearly  $10\%$  for  $1000\times$  solar metallicity. As metallicity increases, the  $\text{H}_2\text{O}$  abundance is also expected to rise to mole fractions comparable to or exceeding the  $\text{CO}_2$  mole fraction (Figure 13). As can be seen in Figure 11, the  $1\sigma$  credible range for the  $\text{H}_2\text{O}$  mole fraction inferred by the SCARLET free chemistry retrieval does indeed extend to nearly  $10\%$ , as is expected for metallicity between 100 and  $1000\times$  solar (Figure 13). However, the corresponding range for the  $\text{H}_2\text{O}$  mole fraction inferred by the petitRADTRANS retrieval extends up to only  $\sim 1\%$  (Table 4) and would suggest a metallicity  $<100\times$  solar. This appears to be in tension with the good match to the data obtained for the chemical equilibrium models with metallicities  $>300\times$  solar (Section 5.1) and could possibly indicate that the petitRADTRANS retrieval has underestimated the  $\text{H}_2\text{O}$  abundance.



**Figure 11.** Posterior distributions inferred for the free parameters of the SCARLET retrieval with unconstrained chemistry. Diagonal panels show the fully marginalized distribution for each parameter, with vertical dashed lines showing the median and  $1\sigma$  credible ranges. Off-diagonal panels show the marginalized posterior distributions for each pair of model parameters. Contours and shading indicate the  $1\sigma$ ,  $2\sigma$ , and  $3\sigma$  credible regions.

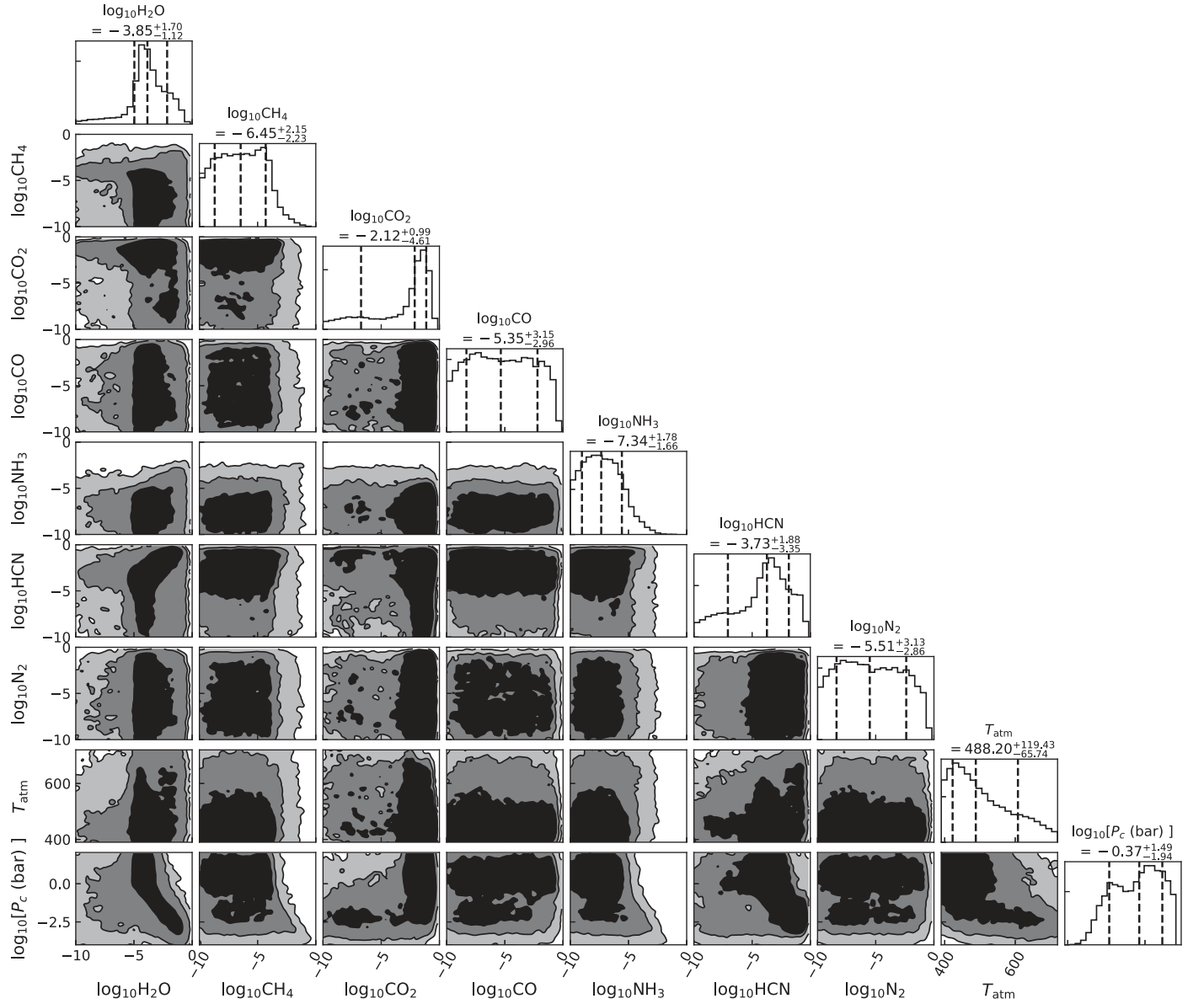
## 6. Interior Structure Modeling

To evaluate the implications of our results for the interior structure of HD 3167c, we take the approach of Thorngren & Fortney (2019) to construct structure evolution models matched to the observed parameters of the planet. Briefly, these models solve the equations of hydrostatic equilibrium, mass conservation, and an equation of state in one spherically symmetric dimension to determine the radius from the mass, composition, and envelope specific entropy. The envelope entropy is evolved over time from a hot initial state using the atmosphere models of Fortney et al. (2007) to regulate cooling. A detailed description of this model can be found in Thorngren et al. (2016).

For simplicity, we assume a two-layer (core and envelope) model and consider two bracketing cases for the core composition: a convective water core and an isothermal olivine-iron core in an Earth-like 2-to-1 ratio (as in Lopez &

Fortney 2014). For our equations of state we use Chabrier et al. (2019) for H/He, Mazevet et al. (2019) for the convective water layer, ANEOS (Thompson 1990) for the envelope ices and core rock (represented by olivine), and SESAME (Lyon & Johnson 1992) for the core iron. The H/He envelope is approximated as fully adiabatic. Although sub-Neptunes may have composition gradients that cause semiconvection in some regions, the fully convecting envelope approximation has produced good results for Neptune (Fortney & Nettelmann 2010) and has been usefully applied to other sub-Neptunes (Nettelmann et al. 2011; Lopez & Fortney 2014).

For HD 3167c, we adopt the following properties: radius  $2.77 \pm 0.20 R_{\oplus}$  (Table 1), mass  $9.8 \pm 1.3 M_{\oplus}$  (Christiansen et al. 2017), and age  $6.7 \pm 0.8$  Gyr (Section 4). We then use MCMC to estimate the core mass required to match these properties as a function of atmospheric envelope metallicity. The results are shown in Figure 14. Note that the atmospheric metallicity results from the transmission spectrum are not used



**Figure 12.** Similar to Figure 11, showing the posterior distributions obtained for the petitRADTRANS free chemistry retrieval analysis. Contours and shading indicate the  $1\sigma$ ,  $2\sigma$ , and  $3\sigma$  credible regions.

**Table 4**  
Free Chemistry Retrieval Prior and Posterior Distributions

Parameter	Unit	Prior	SCARLET	petitRADTRANS
$T_{\text{atm}}$	K	$\mathcal{U}(400, 800)$	$558^{+109}_{-108}$	$488^{+119}_{-66}$
$\log_{10} P_c$	bar dex	$\mathcal{U}(-8, 2)$	$-0.9^{+1.9}_{-2.0}$	$-0.4^{+1.5}_{-1.9}$
Mole Fractions				
$\log_{10}\text{H}_2\text{O}$	dex	$\mathcal{U}(-10, 0)$	$-3.6^{+2.3}_{-3.4}$	$-3.8^{+1.7}_{-1.1}$
$\log_{10}\text{HCN}$	dex	$\mathcal{U}(-10, 0)$	$-1.6^{+1.0}_{-4.3}$	$-3.7^{+1.9}_{-3.4}$
$\log_{10}\text{CO}_2$	dex	$\mathcal{U}(-10, 0)$	$-4.1^{+2.5}_{-3.9}$	$-2.1^{+1.0}_{-4.6}$
$\log_{10}\text{CO}$	dex	$\mathcal{U}(-10, 0)$	$-5.0^{+3.3}_{-3.3}$	$-5.3^{+3.1}_{-3.0}$
$\log_{10}\text{N}_2$	dex	$\mathcal{U}(-10, 0)$	$-5.0^{+3.3}_{-3.3}$	$-5.5^{+3.1}_{-2.9}$
$\log_{10}\text{CH}_4$	dex	$\mathcal{U}(-10, 0)$	$-5.9^{+2.7}_{-2.7}$	$-6.5^{+2.2}_{-2.2}$
$\log_{10}\text{NH}_3$	dex	$\mathcal{U}(-10, 0)$	$-7.0^{+2.2}_{-1.9}$	$-7.3^{+1.8}_{-1.7}$

directly in the model but help us to interpret the result, as upward-convecting envelope material becomes atmosphere

material. In particular, the transmission spectrum favors atmospheric metallicities up to  $1000\times$  solar (Figure 10). We find that for atmospheric envelope metallicities across this range, HD 3167c must have a core mass fraction of at least  $\sim 40\%$  for a rock-dominated core and at least  $\sim 60\%$  for a water-dominated core at the  $1\sigma$  level (Figure 14). The real core is probably a mixture of these, and so its minimum mass likely lies between these two limiting cases.

## 7. Discussion

The HST transmission spectrum presented here for HD 3167c adds to a modest sample acquired to date for sub-Neptunes above the radius valley, with radii between  $1.8$  and  $4R_{\oplus}$ . As shown in Figure 15, the other sub-Neptunes are GJ 1214b (Kreidberg et al. 2014), 55 Cnc e (Tsiaras et al. 2016), HD 97658b (Guo et al. 2020), and K2-18b (Benneke et al. 2019b). In addition to those shown in Figure 15, there have been a few spectra published for planets somewhat larger

**Table 5**  
Bayesian Model Comparison Results for the SCARLET and  
petitRADTRANS Free Chemistry Retrieval Analyses

SCARLET			petitRADTRANS		
Model	$B$	$N_\sigma$	Model	$B$	$N_\sigma$
H <sub>2</sub> O, CH <sub>4</sub> , HCN excluded	9.6	2.7	H <sub>2</sub> O, CO <sub>2</sub> , HCN excluded	7.4	2.5
HCN excluded	2.5	2.0	H <sub>2</sub> O, CO <sub>2</sub> , CH <sub>4</sub> excluded	6.3	2.5
H <sub>2</sub> O, CH <sub>4</sub> excluded	2.1	1.8	H <sub>2</sub> O, HCN excluded	5.9	2.4
H <sub>2</sub> O excluded	1.8	1.7	H <sub>2</sub> O, CO <sub>2</sub> excluded	5.9	2.4
CO <sub>2</sub> excluded	1.2	1.4	H <sub>2</sub> O, CH <sub>4</sub> excluded	5.4	2.4
CO excluded	1.1	1.1	H <sub>2</sub> O, CH <sub>4</sub> , HCN excluded	3.4	2.2
N <sub>2</sub> excluded	1.0	1.0	H <sub>2</sub> O, NH <sub>3</sub> excluded	2.3	1.9
All absorbers included	1.0	0.9	CH <sub>4</sub> , HCN excluded	1.7	1.7
CH <sub>4</sub> excluded	0.9	0.9	H <sub>2</sub> O excluded	1.5	1.6
NH <sub>3</sub> excluded	0.6	0.9	HCN excluded	1.5	1.6
			HCN, NH <sub>3</sub> excluded	1.5	1.6
			CO <sub>2</sub> , NH <sub>3</sub> excluded	1.4	1.6
			CO excluded	1.3	1.5
			CH <sub>4</sub> , CO <sub>2</sub> excluded	1.2	1.3
			All absorbers included	1.0	0.9
			CO <sub>2</sub> excluded	0.6	0.9
			NH <sub>3</sub> excluded	0.6	0.9
			CH <sub>4</sub> excluded	0.6	0.9
			CH <sub>4</sub> , NH <sub>3</sub> excluded	0.6	0.9

**Note.**  $B$  is the Bayes factor, giving the relative likelihood of the model with all gas absorbers included to the listed model with a subset of absorbers removed.  $N_\sigma$  gives the corresponding statistical significance under the frequentist paradigm, following Trotta (2008).

than Neptune ( $4\text{--}5 R_\oplus$ ), namely, HAT-P-11b (Fraine et al. 2014), GJ 436b (Knutson et al. 2014a), GJ 3470b (Benneke et al. 2019a), and HD 106315c (Kreidberg et al. 2020). Already, the diversity predicted for the atmospheric properties of this population (e.g., Elkins-Tanton & Seager 2008; Fortney et al. 2013) is being borne out by observations, reminiscent of that which has been well documented for the hot Jupiters (e.g., Sing et al. 2016).

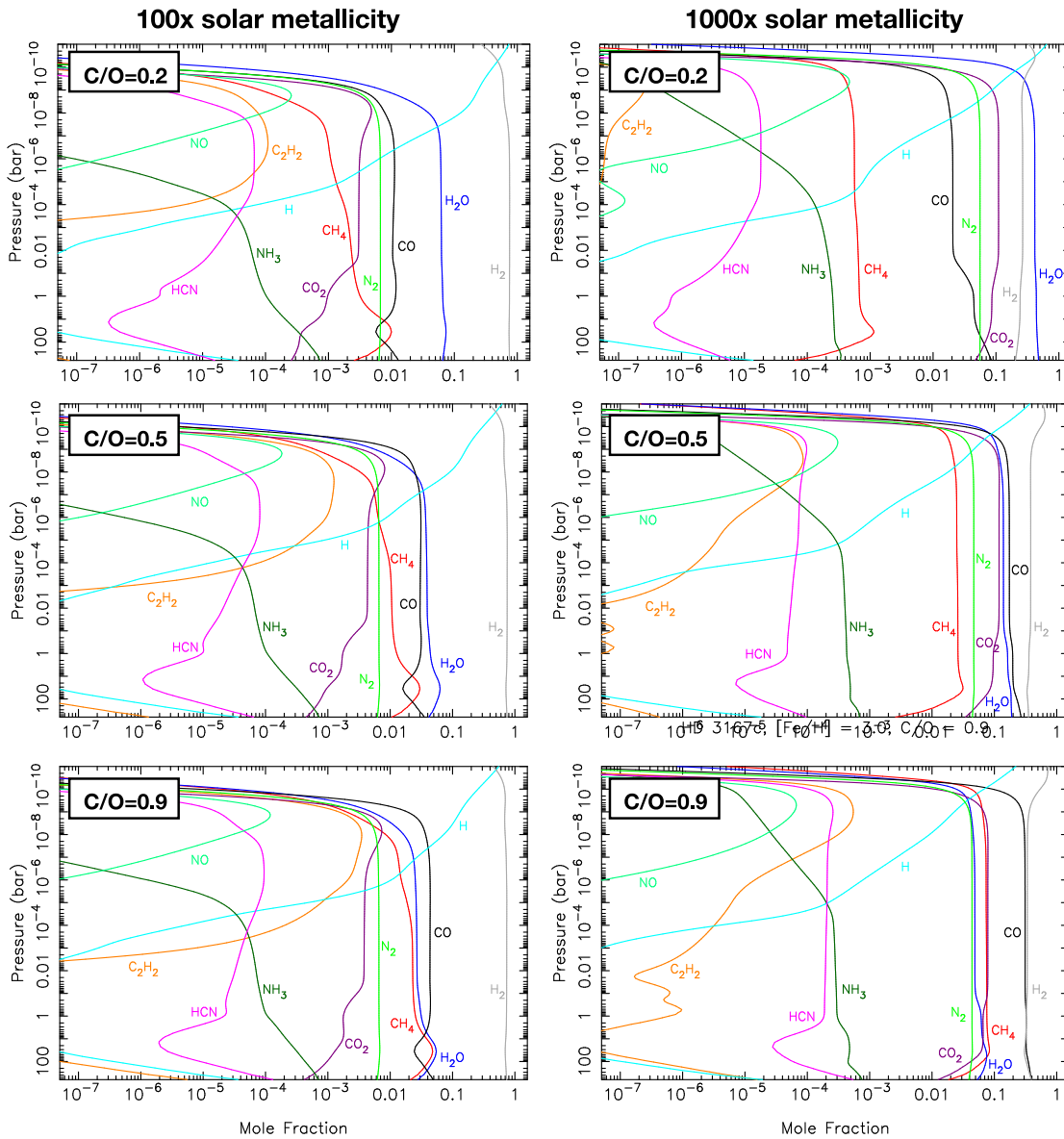
As described in Section 5, the currently available data do not allow us to discriminate between high-metallicity and cloudy atmosphere scenarios for HD 3167c. However, due to the sensitivity of transmission spectra to even trace amounts of cloud (Fortney 2005), this degeneracy is a widespread issue that affects not only other Neptune-sized planets (e.g., Benneke et al. 2019b; Kreidberg et al. 2020) but also many hot Jupiters (e.g., Benneke 2015).

For the composition of a putative cloud layer, broadly speaking there are two possibilities: equilibrium condensates and photochemical hazes. Given the temperature of HD 3167c, the most likely equilibrium condensate is KCl, which was proposed by Morley et al. (2012) as an important cloud species in the atmospheres of T dwarfs. Indeed, for all but the highest metallicities ( $<1000\times$  solar), the PT profile of HD 3167c is expected to first cross the KCl condensation curve at pressures  $\lesssim 1$  bar (Figure 7), coinciding with pressures probed by the transmission spectrum (e.g., Mollière et al. 2019). The PT profile is also expected to cross the condensation curve of ZnS (Figure 7), which was suggested by Morley et al. (2012) as another potentially important cloud species. However, recent modeling work by Gao et al. (2020) suggests that the formation

of significant ZnS cloud mass is challenging, owing to high nucleation energy barriers. In the same study, Gao et al. note that although the formation of KCl clouds should be efficient, at temperatures below 950 K photochemical haze is likely to be the dominant aerosol opacity source. This is due to the increasing abundance of CH<sub>4</sub> under chemical equilibrium, which can be photodissociated by incoming UV photons to generate hydrocarbon haze (e.g., Morley et al. 2015; Kawashima & Ikoma 2018, 2019).

It is interesting to compare HD 3167c with GJ 1214b, as these two planets have similar radii and temperatures (Figure 15). Although the GJ 1214b transmission spectrum measured with WFC3 (Kreidberg et al. 2014) is not as precise as that presented here for HD 3167c (Table 2), the smaller radius of GJ 1214 ( $0.201^{+0.004}_{-0.003} R_\odot$ ; Berta et al. 2012) relative to HD 3167 ( $0.872 \pm 0.057 R_\odot$ ; Christiansen et al. 2017) results in tighter constraints for the atmospheric properties of the former. Specifically, the only plausible explanation for the lack of spectral features detected in the GJ 1214b spectrum is a high-altitude aerosol layer (Kreidberg et al. 2014; Morley et al. 2015). However, we find  $2.5\sigma$  evidence for molecular absorption in the HD 3167c transmission spectrum (Section 5.3.3), suggesting that if a cloud is present it does not extend as high in the atmosphere as for GJ 1214b. The fact that HD 3167c is about 50% more massive ( $9.80^{+1.30}_{-1.24} M_\oplus$ ; Christiansen et al. 2017) than GJ 1214b ( $6.26 \pm 0.86 M_\oplus$ ; Harpsøe et al. 2013) may provide a clue to understanding this difference. The higher gravitational acceleration could result in an increased sedimentation efficiency for photochemical hazes formed in upper layers of the atmosphere and/or a reduced eddy diffusion coefficient ( $K_{zz}$ ) for mixing equilibrium condensates from deeper layers of the atmosphere. Also worth mentioning in this regard is Kepler-51b, which has a similar equilibrium temperature ( $543 \pm 11$  K; Masuda 2014) to HD 3167c and GJ 1214b, and with a mass of  $2.1^{+1.5}_{-0.8} M_\oplus$  (Masuda 2014), it could reasonably be considered a sub-Neptune. However, with a radius of  $7.1 \pm 0.3 R_\oplus$  (Masuda 2014), Kepler-51b is significantly larger than Neptune and thus has a much lower density than both HD 3167c and GJ 1214b. As for GJ 1214b, the measured transmission spectrum is featureless, implying a high-altitude aerosol layer (Libby-Roberts et al. 2020), which would be consistent with the picture that lower-density planets are more likely to have photochemical hazes persist at high altitudes, or equilibrium condensates lofted from deeper layers.

The reality is undoubtedly more complicated. The hot Jupiters, for which more transmission spectra have been measured, exhibit no discernible correlation between bulk properties such as mass, radius, and temperature and the presence of equilibrium condensates (Sing et al. 2016). We might expect the atmospheric properties of sub-Neptunes to exhibit a similar level of stochasticity. Along these lines, Kawashima & Ikoma (2018, 2019) have highlighted how photochemical haze production sensitively depends on numerous factors, such as the host star UV spectrum, atmospheric metallicity, and C/O ratio, as well as variations in vertical mixing efficiencies. Existing sub-Neptune observations provide only a limited ability to constrain models in this multi-dimensional parameter space. Only by continuing to acquire additional observations for a larger sample of sub-Neptunes might this situation be rectified, while at present it seems impossible to predict the degree to which a given transmission



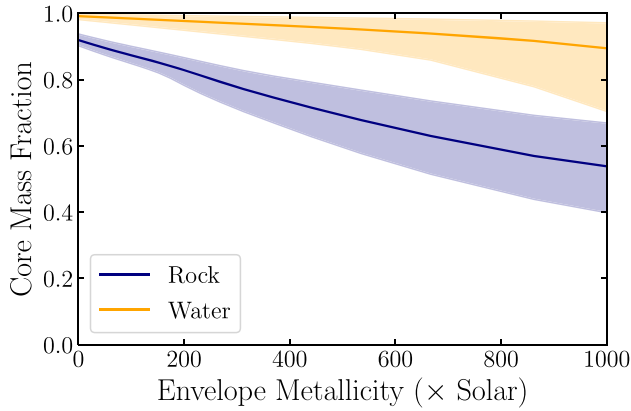
**Figure 13.** Pressure-dependent chemical abundances computed by the thermochemical–photochemical kinetics and transport code described in the text, for a range of metallicities and C/O values.

spectrum will be affected by aerosols prior to observations being made.

Aside from allowing for an aerosol layer, the transmission spectrum is consistent with high metallicities of  $\sim 100$ – $1000\times$  solar (Figure 10). On this point, the hint of  $\text{CO}_2$  inferred by the `petitRADTRANS` retrieval is perhaps worth flagging (Section 5.3.3), as  $\text{CO}_2$  is expected to become an important absorber at high metallicities (Moses et al. 2013). However, it must be reiterated that the indication of  $\text{CO}_2$  in the existing data is extremely tentative, particularly since the `SCARLET` retrieval did not favor its presence (Table 5). Unfortunately, the uncertainty on the IRAC transit depth is too large to make out the strong  $\text{CO}_2$  absorption band in the  $4$ – $5\ \mu\text{m}$  wavelength range, if it is present (see, e.g., Spake et al. 2019). Observations made with either the `NIRSpec` or `NIRCAM` instrument on the James Webb Space Telescope should shed conclusive light on this (e.g., Greene et al. 2016).

## 8. Conclusion

We have presented a transmission spectrum for the warm Neptune HD 3167c measured using HST WFC3, combined with broadband K2 and IRAC photometry. Our results rule out cloud-free models with metallicities  $< 100\times$  solar at high confidence. Instead, the data can be well explained by cloud-free equilibrium chemistry models with metallicities  $> 700\times$  solar. However, when clouds are considered, the data are also consistent with much lower metallicities, including subsolar. We find evidence for at least one of  $\text{H}_2\text{O}$ ,  $\text{CO}_2$ ,  $\text{HCN}$ , and/or  $\text{CH}_4$  at the equivalent of  $2.5\sigma$  significance when using free chemistry retrievals. However, the available data do not allow the unambiguous identification of any single gas species in the data. We found that the broad allowed ranges for all considered gas species are consistent with predictions made by self-consistent models that account for photochemistry and vertical mixing. Two-layered interior structure modeling suggests that the core mass fraction is at least 40%, independent of the



**Figure 14.** Core mass fractions implied by a two-layer interior structure model for a range of atmospheric envelope metallicities. As described in the text, the limiting cases are considered: a pure water core (orange) and a rocky core with a 2-to-1 olivine-to-iron composition (purple). In both cases, the atmospheric envelope is H/He dominated. Shaded regions indicate  $1\sigma$  credible ranges.

assumed core composition and atmospheric envelope metallicities up to  $1000\times$  solar.

The authors are grateful to the referee for constructive feedback that improved the quality of the manuscript. Support for HST program GO-15333 was provided by NASA through a grant from the Space Telescope Science Institute, which is operated by the Association of Universities for Research in Astronomy, Inc., under NASA contract NAS 5-26555. This work is based in part on observations made with the Spitzer Space Telescope, which was operated by the Jet Propulsion Laboratory, California Institute of Technology, under a contract with NASA. This research has made use of the SIMBAD database, operated at CDS, Strasbourg, France. Some of the data presented in this paper were obtained from the Mikulski Archive for Space Telescopes (MAST). STScI is operated by the Association of Universities for Research in Astronomy, Inc., under NASA contract NAS5-26555. Support for MAST for non-HST data is provided by the NASA Office of Space Science via grant NNX13AC07G and by other grants and contracts. P.M. acknowledges support from the European Research Council under the European Union’s Horizon 2020 research and innovation program under grant agreement No. 832428. D.D. acknowledges support from the TESS Guest Investigator Program grant 80NSSC19K1727 and NASA Exoplanet Research Program grant 18-2XRP18 2-0136. M.R. K. is supported by the NSF Graduate Research Fellowship, grant No. DGE 1339067.

*Facilities:* HST(WFC3), Spitzer(IRAC), Kepler(K2), Keck (HIRES).

*Software:* NumPy (van der Walt et al. 2011), SciPy (Virtanen et al. 2020), Matplotlib (Hunter 2007), emcee (Foreman-Mackey et al. 2013), batman (Kreidberg 2015), Astropy (Astropy Collaboration et al. 2013, 2018), pysynphot (STScI Development Team 2013), petitRadtrans (Mollière et al. 2019), PyMultinest (Buchner et al. 2014).

## Appendix A Data Reduction: HST WFC3

We used the IMA files produced by the *calwf3* pipeline version 3.5.0, which already have basic calibrations such as

flat-fielding and bias subtraction applied. The target flux was extracted from each exposure by taking the difference between successive nondestructive reads. To do this, we first estimated and subtracted the background flux for each read, by taking the median pixel count within the box defined by cross-dispersion rows 20–40 and dispersion columns 100–300 (Figure 16). Typical background levels per pixel integrated over the full 70 s exposures were  $\sim 430 e^-$  for G141v1,  $\sim 140 e^-$  for G141v2,  $\sim 230 e^-$  for G141v3,  $\sim 130 e^-$  for G141v4, and  $170 e^-$  for G141v5 (Figure 1). We also experimented with background estimates obtained using different boxes located away from the target spectrum, but we found the count levels to be similar with no appreciable effect on the final results.

For each read-difference frame, we then determined the flux-weighted center of the scanned spectrum along the cross-dispersion axis. All pixel values located more than 130 pixels above and below this row were set to zero, effectively removing flux contributions from nearby contaminant stars and cosmic-ray strikes outside a rectangular aperture. We note, however, that visual inspection of the data frames did not suggest any apparent contamination of the target scans by nearby stars (Figure 16). This is supported by ground-based direct imaging observations, which place deep limits on the minimum contrast of any nearby stars within  $3''$  of HD 3167 (Vanderburg et al. 2016; Christiansen et al. 2017; Ligi et al. 2018),<sup>33</sup> and visual inspection of the HST acquisition images for wider separations. Final reconstructed frames were produced by adding together the read-differences produced in this manner. During this process, we also estimated how the spectrum drifted across the detector over the course of the observations. For all visits, we found that the scanned spectrum drifted by no more than  $\sim 0.1$  pixels along the dispersion axis and  $\sim 0.2$  pixels along the cross-dispersion axis (Figure 1).

The target spectrum was then extracted from each frame by summing the flux within a rectangular aperture spanning the full dispersion axis and 380 pixels along the cross-dispersion axis, centered on the central cross-dispersion row of the scan (Figure 16). Before settling on this aperture size, we experimented with other apertures ranging from 300 to 400 pixels and determined that this choice had a negligible effect on our final results. The wavelength solution was determined by cross-correlating each of the spectra extracted with the 380-pixel aperture against a model stellar spectrum modulated by the throughput of the G141 grism, as in Evans et al. (2016, 2017). For the stellar spectrum, we used the *pysynphot* Python package (STScI Development Team 2013) to interpolate the Kurucz (1993) model grid for properties appropriate to the HD 3167 host star.

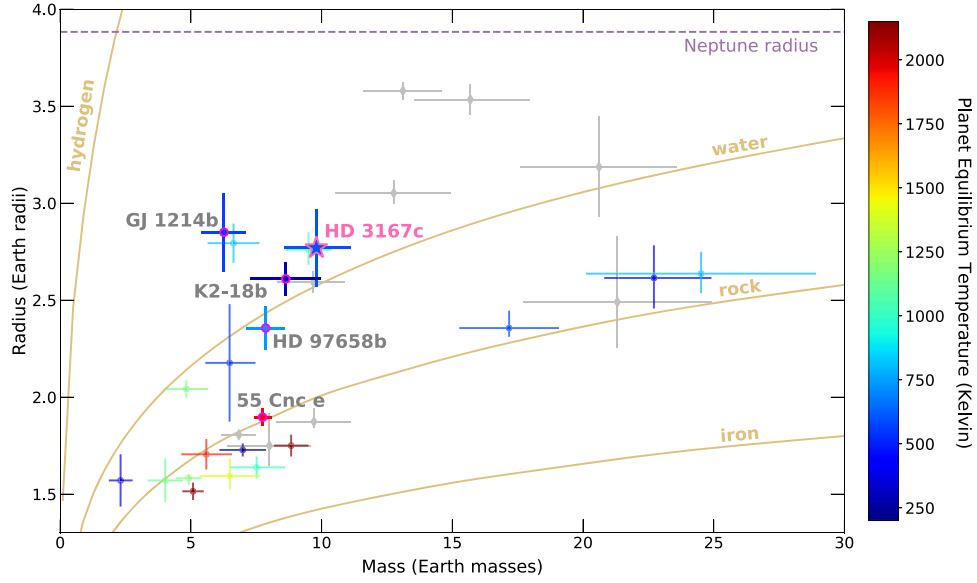
## Appendix B Fitting the HST WFC3 Broadband Light Curve

Following standard practice, we discarded the entire first HST orbit of each visit and the first round-trip scan of each subsequent orbit from our analysis, as these are affected by especially strong systematics. We then fit all light curves simultaneously, defining a log-likelihood function of the form

$$\ln p = \sum_i^N \ln p_i, \quad (\text{B1})$$

<sup>33</sup> See, e.g., Figure 1 of Ligi et al. (2018).





**Figure 15.** Masses and radii for known sub-Neptunes and super-Earths. Error bars show  $1\sigma$  measurement uncertainties. Only planets with published masses measured to better than 20% precision are shown. Colored markers indicate planets orbiting bright stars ( $J < 10$  mag), typically a prerequisite for atmosphere characterization observations, while gray diamonds indicate fainter systems. The color scale for bright systems corresponds to planet equilibrium temperature, assuming zero Bond albedo and uniform heat redistribution from dayside to nightside hemispheres. Light-brown contours are for 100% iron, rock, water, and hydrogen compositions. The five sub-Neptunes with published HST transmission spectra are labeled and highlighted by pink halos.

where  $p_i$  is the log-likelihood of the  $i$ th data set. For the latter, we assumed a GP log-likelihood of the form

$$\ln p_i \sim \ln \mathcal{N}(\boldsymbol{\mu}_i, \boldsymbol{\Sigma}_i), \quad (\text{B2})$$

where  $\mathcal{N}$  is a Gaussian distribution with deterministic mean function  $\boldsymbol{\mu}_i$  and covariance matrix  $\boldsymbol{\Sigma}_i$ . For  $\boldsymbol{\mu}_i$ , we used

$$\boldsymbol{\mu}_i = \begin{cases} f_i M(t; \boldsymbol{\alpha}_i) R(t, \phi; \boldsymbol{\gamma}_i) & \text{for forward scans} \\ b_i M(t; \boldsymbol{\alpha}_i) R(t, \phi; \boldsymbol{\gamma}_i) & \text{for backward scans} \end{cases} \quad (\text{B3})$$

where  $t$  is time;  $\phi$  is HST orbital phase;  $f_i$  and  $b_i$  are normalization constants for the two spatial-scan directions;  $M$  is a transit function, which we implemented using the `batman` Python package (Kreidberg 2015); and  $R$  is an analytic model for the WFC3 detector systematics, described below.

The transit function was parameterized by  $\boldsymbol{\alpha}_i = [R_p/R_*, T_i]$ , with the planet-to-star radius ratio ( $R_p/R_*$ ) shared across all five data sets, while the transit midtimes ( $T_i$ ) were allowed to vary separately for each data set. We experimented with allowing the stellar limb-darkening coefficients to vary as free parameters and holding them fixed to values determined from stellar models. We found that this choice did not affect the final results, and so we adopted a quadratic limb-darkening law with coefficients ( $u_1, u_2$ ) fixed to values computed using the online ExoCTK tool.<sup>34</sup> As noted in Section 3.1, we also fixed the normalized semimajor axis ( $a/R_*$ ) and orbital impact parameter ( $b$ ) to the values listed in Table 1, obtained from a global fit to all available K2 and Spitzer data for HD 3167b and HD 3167c (K. K. Hardegree-Ullman et al. 2020, in preparation). We note that these values are within the  $1\sigma$  credible ranges reported by both Christiansen et al. (2017) and Gandolfi et al. (2017). The planetary orbital period was fixed to  $P = 29.84622$  days, as reported by Gandolfi et al. (2017). We assumed a circular orbit, given the lack of compelling evidence for a nonzero eccentricity

(Christiansen et al. 2017; Gandolfi et al. 2017) and the minimal impact it has on the shape of the transit at the level of data precision.

For the deterministic component of the detector systematics, we used an analytic ramp model almost identical to that introduced by de Wit et al. (2018), given by

$$R(t, \phi; \boldsymbol{\gamma}) = r_v(t; \gamma_1, \gamma_2) r_o(\phi; \gamma_3, \gamma_4, \gamma_5), \quad (\text{B4})$$

where

$$r_v(t; \gamma_1, \gamma_2) = 1 + \gamma_1 \exp[-\gamma_2 t] \quad (\text{B5})$$

and

$$r_o(\phi; \gamma_3, \gamma_4, \gamma_5) = 1 + \gamma_3 \exp\left[-\left(\frac{\phi - \gamma_5}{\gamma_4 r_v}\right)^2\right]. \quad (\text{B6})$$

We also used the covariance matrix  $\boldsymbol{\Sigma}_i$  to encode additional systematics and noise properties of the data. The  $jk$ th entry was defined by

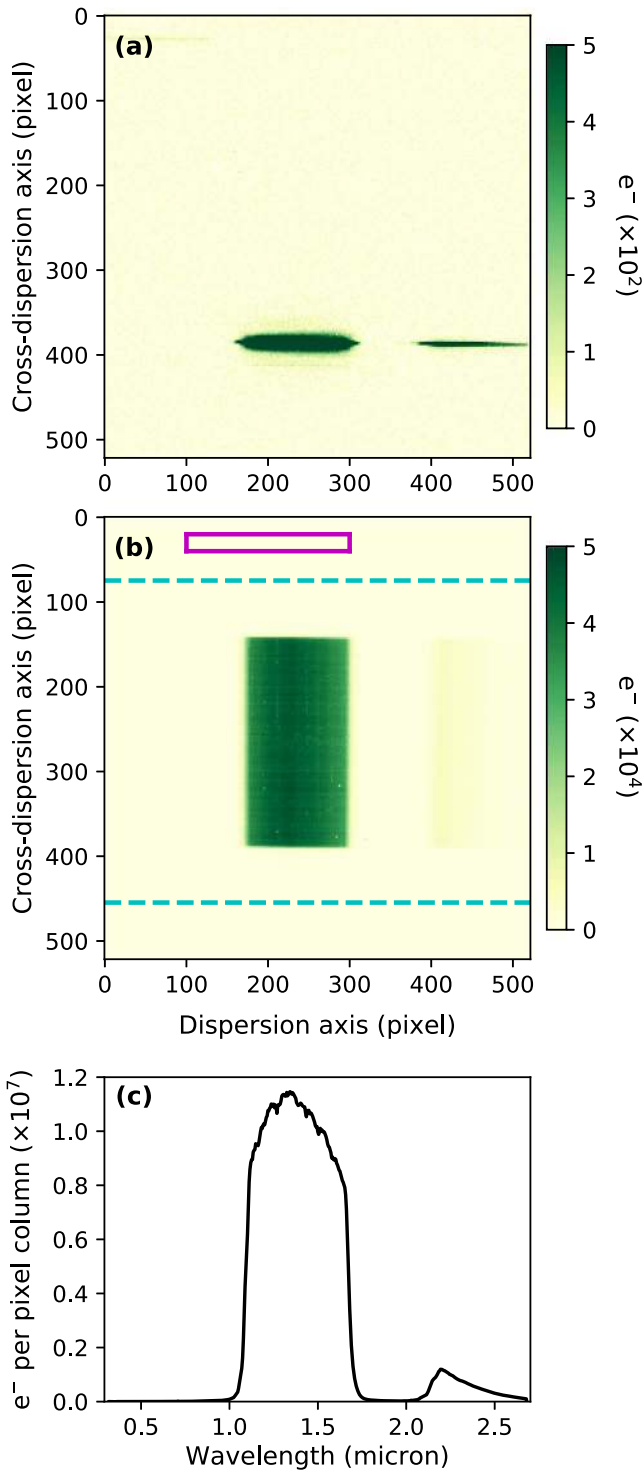
$$\boldsymbol{\Sigma}_{ijk} = K_{\text{SE}}(t_j, t_k; A_{t,i}, \eta_{t,i}) + K_{\text{SE}}(\phi_j, \phi_k; A_{\phi,i}, \eta_{\phi,i}) + \delta_{jk} \beta_i^2 \sigma_i^2, \quad (\text{B7})$$

where  $\delta_{jk}$  is the Kronecker delta,  $\sigma_i$  is the photon noise value, and  $K_{\text{SE}}$  denotes a squared-exponential covariance kernel of the form

$$K_{\text{SE}}(\epsilon_j, \epsilon_k; A, \eta) = A^2 \exp\left[-\frac{1}{2} \eta^2 (\epsilon_j - \epsilon_k)^2\right], \quad (\text{B8})$$

where  $A$  is the covariance amplitude and  $\eta$  is the inverse correlation length scale. In Equation (B7), the first  $K_{\text{SE}}$  kernel was employed to capture the  $t$ -dependent baseline trend for each visit. The second  $K_{\text{SE}}$  kernel was included to account for any systematics repeating from orbit to orbit not captured by the analytic ramp model given by Equation (B4). Finally, the  $\beta_i$  term allows for the uncorrelated noise value to be higher than the formal photon noise  $\sigma_i$ , which is useful if additional high-

<sup>34</sup> <https://exoctk.stsci.edu>



**Figure 16.** (a) First nondestructive read for an example IMA frame. Color scale has been stretched to highlight the lack of neighboring spectra overlapping the target spectrum. The first-order spectrum of HD 3167 spans dispersion columns 170–300, and the fainter second-order spectrum spans columns 390–520. (b) Final nondestructive read of the same IMA frame. Dashed cyan lines indicate the photometric aperture, which was summed along the cross-dispersion axis. Background counts were obtained by taking the median within the purple box. (c) Corresponding 1D spectrum as integrated electron counts vs. wavelength.

frequency noise sources are present in the data that can be approximated as white.

We note in particular that the  $t$ -dependent  $K_{SE}$  kernel used for the baseline trend is significantly more flexible than the low-order polynomial trends that are typically adopted for WFC3 light-curve analyses (e.g., Fraine et al. 2014; Knutson et al. 2014a; Kreidberg et al. 2014, 2020; Evans et al. 2016, 2017; Benneke et al. 2019a, 2019b). This was motivated by a visual inspection of the visit-long trends in the broadband light curves, which do not appear to be well approximated by a low-order  $t$ -dependent polynomial. This is unsurprising given the long duration of the transit, resulting in individual visit durations of  $\sim 8.5$  hr after discarding the first HST orbit. A similar effect was noted by Guo et al. (2020) and Colón et al. (2020) for transit observations of HD 97658b and KELT-11b, respectively. Those authors demonstrated how the broadband  $R_p/R_*$  level varied significantly when different analytic expressions were assumed for the baseline trend, including linear, quadratic, logarithmic, and exponential functions of time. Our approach of using a flexible  $t$ -dependent GP for the baseline trend attempts to address this by marginalizing across a broad function space.

For the  $A_{i,\phi}$  parameters, we adopted Gamma priors of the form  $p(A_{i,\phi}) \propto \exp[-10A_{i,\phi}]$ , while for the  $A_{i,t}$  parameters, we adopted stronger priors of the form  $p(A_{i,t}) \propto \exp[-100A_{i,t}]$ . This was done to prevent the  $t$ -dependent GP baseline from being too flexible and completely degenerate with the transit signal. As in previous work, we fit for the natural logarithm of the inverse correlation length scales ( $\ln \eta_{t,i}$ ,  $\ln \eta_{\phi,i}$ ). For these parameters, as well as all remaining free parameters, we assumed uniform priors.

### Appendix C

#### Fitting the HST WFC3 Spectroscopic Light Curves

For each spectroscopic channel, we fit the corresponding light curves for all five visits simultaneously, adopting a similar GP methodology to that described in Appendix B for the broadband light curve. However, since the common-mode correction removed most of the systematics prior to light-curve fitting, we adopted a somewhat simplified model, with mean function and covariance matrix for the  $i$ th data set defined by

$$\mu_i = \begin{cases} (f_i + m_i t) M(t; \alpha_i) & \text{for forward scans} \\ (b_i + m_i t) M(t; \alpha_i) & \text{for backward scans} \end{cases} \quad (\text{C1})$$

and

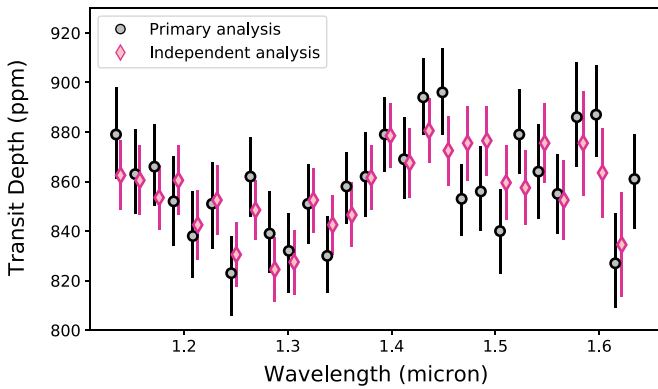
$$\Sigma_{ijk} = K_{SE}(\phi_j, \phi_k; A_{\phi,i}, \eta_{\phi,i}) + \delta_{jk} \beta_i^2 \sigma_i^2. \quad (\text{C2})$$

In particular, we replace the  $t$ -dependent  $K_{SE}$  kernel with a linear- $t$  trend for the baseline and remove the analytic ramp model  $R$ . For the transit signal  $M$ , we also fix the midtimes ( $T_i$ ) to the best-fit values determined for the broadband light curve, leaving  $R_p/R_*$  as the only free parameter for each spectroscopic channel, i.e.,  $\alpha_i = [R_p/R_*]$ . As for the broadband light-curve fit, we adopted a quadratic limb-darkening law and fixed the coefficients to values determined using the ExoCTK tool, which are listed in Table 2. Marginalization was again performed using affine-invariant MCMC.

### Appendix D

#### Independent Analysis of the HST WFC3 Data Set

To verify the WFC3 analysis presented in Sections 2 and 3, a second independent analysis was performed using the method



**Figure 17.** Transmission spectra obtained for HD 3167c from the primary analysis described in Sections 2 and 3 and a second independent analysis employing the methodology of Kreidberg et al. (2014).

of Kreidberg et al. (2014). In brief, we extracted the spectra from each up-the-ramp sample in an exposure using optimal extraction (Horne 1986). The extraction window had a height of 250 pixels. The background was estimated from the median of pixel counts between cross-dispersion rows 6–70 and dispersion columns 450–500. To obtain a final spectrum for each exposure, the up-the-ramp samples were co-added. The data were binned into spectroscopic light curves with similar wavelength spacing to the primary data reduction.

To fit the broadband light curve, we used a transit model together with the `model-ramp` analytic parameterization for the orbit-long systematics described in Kreidberg et al. (2014). We also simultaneously fit a quadratic function of time for the baseline trend of each visit. We then fit the spectroscopic light curves with the `divide-white` common-mode systematics model of Kreidberg et al. (2014). In total, the spectroscopic transit light-curve fits had free parameters for the planet-to-star radius ratio ( $R_p/R_*$ ), a linear limb-darkening parameter ( $u_1$ ), and a visit-long linear slope in time. We obtained uncertainties on the fit parameters with affine-invariant MCMC using the `emcee` Python package (Foreman-Mackey et al. 2013). The uncertainties on the individual data points were rescaled prior to the final MCMC analysis such that the final reduced  $\chi^2$  for the light-curve fit was unity; this increased the size of the error bars by a median of 2%. We confirmed that the spectroscopic light-curve rms bins down with the square root of the number of points per bin, as expected for white, Gaussian-distributed noise. The resulting transmission spectrum is shown in Figure 17 and is in good agreement with the primary analysis.

## Appendix E

### Fitting the Spitzer IRAC Broadband Light Curve

For the mean function, we used

$$\mu = c_0 M(t; \alpha) S(t, f_j; m, c_j), \quad (\text{E1})$$

where  $M$  is a transit model,  $c_0$  is a normalization factor, and  $S$  is a linear decorrelation of the form

$$S = 1 + mt + \sum_{i=1}^9 c_i f_i(t), \quad (\text{E2})$$

where  $m$  is the slope of a linear time trend,  $f_j$  is the time series of the  $j$ th pixel in a  $3 \times 3$  grid centered on the target, and  $c_i$  are associated linear coefficients. Equation (E2) corresponds to the pixel level decorrelation (PLD) framework introduced by

Deming et al. (2015) to account for intrapixel sensitivity variations that generate the dominant systematics in IRAC time series. For the covariance matrix, we used

$$\Sigma_{jk} = K_{\text{SE}}(t_j, t_k; A_t, \eta_t) + \delta_{jk} \beta^2 \sigma^2. \quad (\text{E3})$$

We found that the  $t$ -dependent  $K_{\text{SE}}$  kernel was required to capture residual correlations in the light curve that were not fully corrected by the PLD.

In total, the free parameters of our IRAC light-curve model were  $\alpha = [R_p/R_*, T]$  for the transit signal;  $c_0, m$ , and the nine PLD coefficients  $c_i, A_t$  and  $\eta_t$  for the covariance; and the white-noise rescaling factor  $\beta$ . As for the K2 fit, we applied the WFC3 posterior constraints as Gaussian priors for  $a/R_*$  and  $b$ . For the covariance amplitude, we used a Gamma prior of the form  $p(A_t) \propto \exp[-100A_t]$ . Uniform priors were adopted for the remaining free parameters.

To make the GP likelihood computations tractable, we binned the light curve into 2-minute bins, reducing the size of the data set from  $\mathcal{O}(10^5)$  points to  $\mathcal{O}(10^2)$  points. Marginalization was performed using `emcee`. Preliminary fits indicated that the first  $\sim 2$  hr of the light curve were poorly accounted for by the PLD, so we chose to discard this segment of the light curve in our final analysis. This reduced the pre-transit baseline to approximately 1.8 hr, which was still sufficient to constrain the baseline flux level.

As for the WFC3 analysis, a quadratic limb-darkening law was adopted for both the K2 and IRAC fits, with limb-darkening coefficients fixed to values calculated using the online ExoCTK tool. The latter are listed in Table 2, along with the inferred values for  $R_p/R_*$  and the corresponding transits depths  $(R_p/R_*)^2$ . The systematics-corrected light curves and best-fit transit models for both data sets are shown in Figure 5.

## ORCID iDs

Thomas Mikal-Evans <https://orcid.org/0000-0001-5442-1300>  
 Björn Benneke <https://orcid.org/0000-0001-5578-1498>  
 Laura Kreidberg <https://orcid.org/0000-0003-0514-1147>  
 Julie Moses <https://orcid.org/0000-0002-8837-0035>  
 Caroline V. Morley <https://orcid.org/0000-0002-4404-0456>  
 Daniel Thorngren <https://orcid.org/0000-0002-5113-8558>  
 Paul Mollière <https://orcid.org/0000-0003-4096-7067>  
 Kevin K. Hardegree-Ullman <https://orcid.org/0000-0003-3702-0382>  
 John Brewer <https://orcid.org/0000-0002-9873-1471>  
 Jessie L. Christiansen <https://orcid.org/0000-0002-8035-4778>  
 David R. Ciardi <https://orcid.org/0000-0002-5741-3047>  
 Diana Dragomir <https://orcid.org/0000-0003-2313-467X>  
 Courtney Dressing <https://orcid.org/0000-0001-8189-0233>  
 Jonathan J. Fortney <https://orcid.org/0000-0002-9843-4354>  
 Varoujan Gorjian <https://orcid.org/0000-0002-8990-2101>  
 Thomas P. Greene <https://orcid.org/0000-0002-8963-8056>  
 Lea A. Hirsch <https://orcid.org/0000-0001-8058-7443>  
 Andrew W. Howard <https://orcid.org/0000-0001-8638-0320>  
 Steve B. Howell <https://orcid.org/0000-0002-2532-2853>  
 Howard Isaacson <https://orcid.org/0000-0002-0531-1073>  
 Molly R. Kosiarek <https://orcid.org/0000-0002-6115-4359>  
 Jessica Krick <https://orcid.org/0000-0002-2413-5976>  
 John H. Livingston <https://orcid.org/0000-0002-4881-3620>

Joshua D. Lothringer  <https://orcid.org/0000-0003-3667-8633>  
 Farisa Y. Morales  <https://orcid.org/0000-0001-9414-3851>  
 Erik A. Petigura  <https://orcid.org/0000-0003-0967-2893>  
 Joshua E. Schlieder  <https://orcid.org/0000-0001-5347-7062>

## References

- Adams, E. R., Seager, S., & Elkins-Tanton, L. 2008, *ApJ*, 673, 1160  
 Agúndez, M., Parmentier, V., Venot, O., Hersant, F., & Selsis, F. 2014, *A&A*, 564, A73  
 Alam, M. K., Lopez-Morales, M., Nikolov, N., et al. 2020, *AJ*, 160, 51  
 Arcangeli, J., Désert, J.-M., Parmentier, V., et al. 2019, *A&A*, 625, A136  
 Asplund, M., Grevesse, N., Sauval, A. J., & Scott, P. 2009, *ARA&A*, 47, 481  
 Astropy Collaboration, Price-Whelan, A. M., Sipőcz, B. M., et al. 2018, *AJ*, 156, 123  
 Astropy Collaboration, Robitaille, T. P., Tollerud, E. J., et al. 2013, *A&A*, 558, A33  
 Bate, M. R., Lodato, G., & Pringle, J. E. 2010, *MNRAS*, 401, 1505  
 Batygin, K. 2012, *Natur*, 491, 418  
 Baumeister, P., Padovan, S., Tosi, N., et al. 2020, *ApJ*, 889, 42  
 Benneke, B. 2015, arXiv:1504.07655  
 Benneke, B., Knutson, H. A., Lothringer, J., et al. 2019a, *NatAs*, 3, 813  
 Benneke, B., & Seager, S. 2012, *ApJ*, 753, 100  
 Benneke, B., & Seager, S. 2013, *ApJ*, 778, 153  
 Benneke, B., Wong, I., Piaulet, C., et al. 2019b, *ApJL*, 887, L14  
 Berta, Z. K., Charbonneau, D., Désert, J.-M., et al. 2012, *ApJ*, 747, 35  
 Brewer, J. M., & Fischer, D. A. 2016, *ApJ*, 831, 20  
 Brewer, J. M., Fischer, D. A., Valenti, J. A., & Piskunov, N. 2016, *ApJS*, 225, 32  
 Bruno, G., Lewis, N. K., Alam, M. K., et al. 2020, *MNRAS*, 491, 5361  
 Buchner, J., Georgakakis, A., Nandra, K., et al. 2014, *A&A*, 564, A125  
 Carone, L., Mollière, P., Zhou, Y., et al. 2020, arXiv:2006.05382  
 Carter, A. L., Nikolov, N., Sing, D. K., et al. 2020, *MNRAS*, 494, 5449  
 Chabrier, G., Mazevet, S., & Soubiran, F. 2019, *ApJ*, 872, 51  
 Chachan, Y., Knutson, H. A., Gao, P., et al. 2019, *AJ*, 158, 244  
 Christiansen, J. L., Vanderburg, A., Burt, J., et al. 2017, *AJ*, 154, 122  
 Cloutier, R., & Menou, K. 2020, *AJ*, 159, 211  
 Colón, K. D., Kreidberg, L., Line, M., et al. 2020, *AJ*, 160, 280  
 Crossfield, I. J. M., & Kreidberg, L. 2017a, *AJ*, 154, 261  
 Crossfield, I. J. M., & Kreidberg, L. 2017b, The Atmospheric Diversity of Mini-Neptunes in Multi-planet Systems, HST Proposal id.15333  
 Dai, F., Masuda, K., Winn, J. N., & Zeng, L. 2019, *ApJ*, 883, 79  
 Dalal, S., Hébrard, G., Lecavelier des Étangs, A., et al. 2019, *A&A*, 631, A28  
 de Wit, J., Wakeford, H. R., Lewis, N. K., et al. 2018, *NatAs*, 2, 214  
 Deming, D., Knutson, H., Kammer, J., et al. 2015, *ApJ*, 805, 132  
 Deming, D., Louie, D., & Sheets, H. 2019, *PASP*, 131, 013001  
 Deming, D., Wilkins, A., McCullough, P., et al. 2013, *ApJ*, 774, 95  
 Deming, L. D., & Seager, S. 2017, *JGRE*, 122, 53  
 Dorn, C., Venturini, J., Khan, A., et al. 2017, *A&A*, 597, A37  
 dos Santos, L. A., Ehrenreich, D., Bourrier, V., et al. 2019, *A&A*, 629, A47  
 Dressing, C. D., & Charbonneau, D. 2013, *ApJ*, 767, 95  
 Ehrenreich, D., Bonfils, X., Lovis, C., et al. 2014, *A&A*, 570, A89  
 Elkins-Tanton, L. T., & Seager, S. 2008, *ApJ*, 685, 1237  
 Evans, T. M., Aigrain, S., Gibson, N., et al. 2015, *MNRAS*, 451, 680  
 Evans, T. M., Sing, D. K., Kataria, T., et al. 2017, *Natur*, 548, 58  
 Evans, T. M., Sing, D. K., Wakeford, H. R., et al. 2016, *ApJL*, 822, L4  
 Fazio, G. G. 2004, *ApJS*, 154, 10  
 Foreman-Mackey, D., Hogg, D. W., Lang, D., & Goodman, J. 2013, *PASP*, 125, 306  
 Foreman-Mackey, D., Hogg, D. W., & Morton, T. D. 2014, *ApJ*, 795, 64  
 Fortney, J. J. 2005, *MNRAS*, 364, 649  
 Fortney, J. J., Marley, M. S., & Barnes, J. W. 2007, *ApJ*, 659, 1661  
 Fortney, J. J., Mordasini, C., Nettelmann, N., et al. 2013, *ApJ*, 775, 80  
 Fortney, J. J., & Nettelmann, N. 2010, *SSRv*, 152, 423  
 Fortney, J. J., Shabram, M., Showman, A. P., et al. 2010, *ApJ*, 709, 1396  
 Fraine, J., Deming, D., Benneke, B., et al. 2014, *Natur*, 513, 526  
 Fressin, F., Torres, G., Charbonneau, D., et al. 2013, *ApJ*, 766, 81  
 Fu, G., Deming, D., Lothringer, J., et al. 2020, arXiv:2005.02568  
 Fulton, B. J., Petigura, E. A., Howard, A. W., et al. 2017, *AJ*, 154, 109  
 Gaia Collaboration, Brown, A. G. A., Vallenari, A., et al. 2018, *A&A*, 616, A1  
 Gandolfi, D., Barragán, O., Hatzes, A. P., et al. 2017, *AJ*, 154, 123  
 Gao, P., Thorngren, D. P., Lee, G. K. H., et al. 2020, *NatAs*, 4, 951  
 Greene, T. P., Line, M. R., Montero, C., et al. 2016, *ApJ*, 817, 17  
 Guo, X., Crossfield, I. J. M., Dragomir, D., et al. 2020, *AJ*, 159, 239  
 Gupta, A., & Schlichting, H. E. 2019, *MNRAS*, 487, 24  
 Harpsøe, K. B. W., Hardis, S., Hinse, T. C., et al. 2013, *A&A*, 549, A10  
 Home, K. 1986, *PASP*, 98, 609  
 Howard, A. W., Marcy, G. W., Johnson, J. A., et al. 2010, *Sci*, 330, 653  
 Howe, A. R., Burrows, A., & Verne, W. 2014, *ApJ*, 787, 173  
 Howell, S. B., Sobek, C., Haas, M., et al. 2014, *PASP*, 126, 398  
 Hunter, J. D. 2007, *CSE*, 9, 90  
 Jin, S., & Mordasini, C. 2018, *ApJ*, 853, 163  
 Kawashima, Y., & Ikoma, M. 2018, *ApJ*, 853, 7  
 Kawashima, Y., & Ikoma, M. 2019, *ApJ*, 877, 109  
 Knutson, H. A., Benneke, B., Deming, D., & Homeier, D. 2014a, *Natur*, 505, 66  
 Knutson, H. A., Dragomir, D., Kreidberg, L., et al. 2014b, *ApJ*, 794, 155  
 Komacek, T. D., Showman, A. P., & Parmentier, V. 2019, *ApJ*, 881, 152  
 Kreidberg, L. 2015, *PASP*, 127, 1161  
 Kreidberg, L., Bean, J. L., Désert, J.-M., et al. 2014, *Natur*, 505, 69  
 Kreidberg, L., Mollière, P., Crossfield, I. J. M., et al. 2020, arXiv:2006.07444  
 Kubyskhina, D., Cubillos, P. E., Fossati, L., et al. 2019, *ApJ*, 879, 26  
 Kurucz, R. 1993, ATLAS9 Stellar Atmosphere Programs and 2 km s<sup>-1</sup> Grid, CD-ROM No. 13 (Cambridge, MA: Smithsonian Astrophysical Observatory)  
 Libby-Roberts, J. E., Berta-Thompson, Z. K., Désert, J.-M., et al. 2020, *AJ*, 159, 57  
 Ligi, R., Demangeon, O., Barros, S., et al. 2018, *AJ*, 156, 182  
 Lopez, E. D., & Fortney, J. J. 2013, *ApJ*, 776, 2  
 Lopez, E. D., & Fortney, J. J. 2014, *ApJ*, 792, 1  
 Lothringer, J. D., Benneke, B., Crossfield, I. J. M., et al. 2018, *AJ*, 155, 66  
 Lyon, S. P., & Johnson, J. D. 1992, SESAME: The Los Alamos National Laboratory Equation of State Database, Tech. Rep. LA-UR-92-3407  
 Masuda, K. 2014, *ApJ*, 783, 53  
 Mazevet, S., Licari, A., Chabrier, G., & Potekhin, A. Y. 2019, *A&A*, 621, A18  
 Mikal-Evans, T., Sing, D. K., Goyal, J. M., et al. 2019, *MNRAS*, 488, 2222  
 Mikal-Evans, T., Sing, D. K., Kataria, T., et al. 2020, *MNRAS*, 496, 1638  
 Mollière, P., Wardenier, J. P., van Boekel, R., et al. 2019, *A&A*, 627, A67  
 Morley, C. V., Fortney, J. J., Marley, M. S., et al. 2012, *ApJ*, 756, 172  
 Morley, C. V., Fortney, J. J., Marley, M. S., et al. 2015, *ApJ*, 815, 110  
 Morley, C. V., Knutson, H., Line, M., et al. 2017, *AJ*, 153, 86  
 Moses, J. I. 2014, *RSPTA*, 372, 20130073  
 Moses, J. I., Line, M. R., Visscher, C., et al. 2013, *ApJ*, 777, 34  
 Mousis, O., Deleuil, M., Aguichine, A., et al. 2020, *ApJL*, 896, L22  
 Mulders, G. D., Mordasini, C., Pascucci, I., et al. 2019, *ApJ*, 887, 157  
 Nettelmann, N., Fortney, J. J., Kramm, U., & Redmer, R. 2011, *ApJ*, 733, 2  
 Nissen, P. E., Christensen-Dalsgaard, J., Mosumgaard, J. R., et al. 2020, *A&A*, 640, A81  
 Öberg, K. I., Murray-Clay, R., & Bergin, E. A. 2011, *ApJL*, 743, L16  
 Owen, J. E., & Wu, Y. 2013, *ApJ*, 775, 105  
 Owen, J. E., & Wu, Y. 2017, *ApJ*, 847, 29  
 Parmentier, V., Showman, A. P., & Lian, Y. 2013, *A&A*, 558, A91  
 Petigura, E. A., Marcy, G. W., & Howard, A. W. 2013, *ApJ*, 770, 69  
 Rogers, L. A. 2015, *ApJ*, 801, 41  
 Rogers, L. A., & Seager, S. 2010a, *ApJ*, 712, 974  
 Rogers, L. A., & Seager, S. 2010b, *ApJ*, 716, 1208  
 Sing, D. K., Fortney, J. J., Nikolov, N., et al. 2016, *Natur*, 529, 59  
 Sing, D. K., Lavvas, P., Ballester, G. E., et al. 2019, *AJ*, 158, 91  
 Skilling, J. 2004, in AIP Conf. Ser. 735, Bayesian Inference and Maximum Entropy Methods in Science and Engineering: 24th International Workshop on Bayesian Inference and Maximum Entropy Methods in Science and Engineering, ed. R. Fischer, R. Preuss, & U. V. Toussaint (Melville, NY: AIP), 395  
 Sozzen, K. S., Stevenson, K. B., Sing, D. K., et al. 2020, *AJ*, 159, 5  
 Spake, J. J., Sing, D. K., Wakeford, H. R., et al. 2019, *MNRAS*, in press  
 Stevenson, K. B., & Fowler, J. 2019, Analyzing Eight Years of Transiting Exoplanet Observations Using WFC3's Spatial Scan Monitor, Tech. Rep. WFC3 2019-12  
 STScI Development Team 2013, Pysynphot: Synthetic Photometry Software Package, v0.9.14, Astrophysics Source Code Library, ascl:1303.023  
 Thompson, S. L. 1990, ANEOS Analytic Equations of State for Shock Physics Codes Input Manual, Sandia National Labs, Albuquerque, NM (USA), Tech. Rep. SAND-89-2951  
 Thorngren, D., & Fortney, J. J. 2019, *ApJL*, 874, L31  
 Thorngren, D. P., Fortney, J. J., Murray-Clay, R. A., & Lopez, E. D. 2016, *ApJ*, 831, 64  
 Trotta, R. 2008, *ConPh*, 49, 71  
 Tsiaras, A., Rocchetto, M., Waldmann, I. P., et al. 2016, *ApJ*, 820, 99

- Valencia, D., Guillot, T., Parmentier, V., & Freedman, R. S. 2013, *ApJ*, **775**, 10
- Valencia, D., Sasselov, D. D., & O'Connell, R. J. 2007, *ApJ*, **665**, 1413
- van der Walt, S., Colbert, S. C., & Varoquaux, G. 2011, *CSE*, **13**, 22
- van Eylen, V., Agentoft, C., Lundkvist, M. S., et al. 2018, *MNRAS*, **479**, 4786
- Vanderburg, A., Bieryla, A., Duvv, D. A., et al. 2016, *ApJL*, **829**, L9
- Vanderburg, A., & Johnson, J. A. 2014, *PASP*, **126**, 948
- Virtanen, P., Gommers, R., Oliphant, T. E., et al. 2020, *NatMe*, **17**, 261
- Vogt, S. S., Allen, S. L., Bigelow, B. C., et al. 1994, *Proc. SPIE*, **2198**, 362
- Wakeford, H. R., Sing, D. K., Stevenson, K. B., et al. 2020, *AJ*, **159**, 204
- Weiss, L. M., & Marcy, G. W. 2014, *ApJL*, **783**, L6
- Werner, M., Crossfield, I., Akeson, R., et al. 2016, Spitzer v. K2: Part II, Spitzer Proposal [id. 13052](#)
- Wong, I., Benneke, B., Gao, P., et al. 2020, *AJ*, **159**, 234
- Woods, T. N., & Rottman, G. J. 2002, *GMS*, **130**, 221
- Zahnle, K. J., & Catling, D. C. 2017, *ApJ*, **843**, 122
- Zeng, L., Jacobsen, S. B., Sasselov, D. D., et al. 2019, *PNAS*, **116**, 9723